NOVEL EXPERIMENTAL MEASURING TECHNIQUES REQUIRED TO PROVIDE DATA FOR CFD VALIDATION

H.-M. Prasser

Swiss Federal Institute of Technology Zurich, Mechanical and Process Engineering,
Professor for Nuclear Energy System, E-mail: hprasser@ethz.ch

Forschungszentrum Rossendorf e.V., P.O.Box 510119, D-01314 Dresden, Germany

Abstract

CFD code validation requires experimental data that characterize distributions of parameters within large flow domains. On the other hand, the development of geometry-independent closure relations for CFD codes have to rely on instrumentation and experimental techniques appropriate for the phenomena that are to be modelled, which usually requires high spatial and time resolution. The presentation reports about the use of wire-mesh sensors to study turbulent mixing processes in the single-phase flow as well as to characterize the dynamics of the gas-liquid interface in a vertical pipe flow. Experiments at a pipe of a nominal diameter of 200 mm are taken as the basis for the development and test of closure relations describing bubble coalescence and break-up, interfacial momentum transfer and turbulence modulation for a multi-bubble-class model. This is done by measuring the evolution of the flow structure along the pipe. The transferability of the extended CFD code to more complicated 3D flow situations is assessed against measured data from tests involving two-phase flow around an asymmetric obstacle placed in a vertical pipe. The obstacle, a half-moon-shaped diaphragm, is movable in the direction of the pipe axis; this allows the 3D gas fraction field to be recorded without changing the sensor position. In the outlook, the pressure chamber of TOPFLOW is presented, which will be used as the containment for a test facility, in which experiments can be conducted in pressure equilibrium with the inner atmosphere of the tank. In this way, flow structures can be observed by optical means through large-scale windows even at pressures of up to 5 MPa. The so-called “Diving Chamber” technology will be used for Pressurized Thermal Shock (PTS) tests. Finally, some important trends in instrumentation for multi-phase flows will be given. This includes the state-of-art of X-ray and gamma tomography, new multi-component wire-mesh sensors, and a discussion of the potential of other non-intrusive techniques, such as neutron radiography and Magnetic Resonance Imaging (MRI).

1. Introduction

CFD code validation requires experimental data that characterize distributions of parameters within large flow domains. On the other hand, the development of geometry-independent closure relations for CFD codes have to rely on instrumentation and experimental techniques appropriate for the phenomena that are to be modelled on the different scales. This creates quite a challenge to the instrumentation development. Optical methods have demonstrated to be most powerful in this sense. A prominent example is the use of PIV combined with LIF for bubbly flows. Tracer particles are doted with a luminescent dye to distinguish them from bubbles. In this way, bubble and liquid velocity distributions, and with some limitations also bubble sizes, are measured simultaneously. High-speed PIV allows to get access to turbulence parameters as well, though for local measurements LDA and hot wire / hot film probes are appropriate, too.

Unfortunately, these methods become very soon inapplicable at higher loads of the discrete phase due to the deterioration of the optical access. In fact, CFD modelling of two-phase flows applied to reactor safety problems must be able to cover the entire range of void fractions starting from plain liquid coolant flow via all known flow pattern towards plain steam flow without losing the ability to resolve the scale of the gas-liquid interface. Furthermore, the simulation must include the modelling of local

processes of phase change, independently if it happens at the heated or cooled boundary or due to interfacial heat exchange. The modelling must be robust concerning large changes and large gradients of the physical properties of the fluid, which requires experiments at close-to-reactor conditions.

The paper therefore concentrates on methods, which combine a high spatial and time resolution with the capability to function in a wide void fraction range, in the presence of intensive phase changes and at pressures and temperatures that are close to reactor parameters. The wire-mesh sensor is such a device, although it is intrusive and the influence to the flow cannot be neglected. It is very useful for single phase mixing studies and - which is of particular interest in light-water reactor safety - for experiments with gas-liquid two-phase flows. In the latter case, they are capable in delivering instantaneous gas fraction distributions with such a high resolution, that the shape, volume and partially the velocity of all individual bubbles passing through the measuring cross-section can be evaluated. This allows to obtain numerous important characteristics of the flow, like void fraction profiles, bubble-size distributions, void profiles decomposed into bubble-size classes, gas velocity profiles and some cross-correlations between signals from different locations that reveal information about turbulent dispersion.

It is important and quite a challenge to search for alternative non-intrusive methods that offer at least a similar if not a better resolution. Some progress has been made concerning radiometric methods. It will be shown, that gamma and X-ray tomography can reach and exceed the resolution achieved by wire-mesh sensors, when special measures are taken to speed-up the process of acquisition of projections of the object to be studied. Finally, it will be discussed, to which extend neutron radiography and magnetic resonance imaging are perspective candidates for future two-phase instrumentation developments.

Despite of the progress described above, optical observation of the flow has always a big value for understanding the physical phenomena, and an application of high-speed video observations as well as the initially mentioned laser methods to fluid-dynamic processes at pressures and temperatures typical for power plants is very much desirable. Unfortunately, the optical access becomes increasingly difficult with rising pressure. This was the motivation to develop a novel technique to conduct fluid-dynamic experiments under high-pressures conditions. A pressure chamber is used as the containment for the test facility itself, and is operated in pressure equilibrium with the inner atmosphere of the tank. In this way, flow structures can be observed by optical means through large-scale windows even at pressures of up to 5 MPa. Beside this, test cannels with non-pressurizable geometries (flat channels, segments of downcomers) can be realized, the walls of test components may remain thin, instrumentation becomes easier and costs can be reduced. The so-called “Diving Chamber” technology will be used for hot-leg flow structure studies and Pressurized Thermal Shock (PTS) tests.

CFD is based on a numerical solution of the conservation equations for the phases and components participating in the flow on a grid of calculation nodes that represents the discretized geometry of the flow domain. Indispensable ingredients for a two-phase flow CFD (except in case of DNS) are empirical closure laws describing

- the dynamics of turbulence parameters (also for single-phase flows),
- the interaction of the participating phases (mass, momentum and energy exchange at the gas-liquid interface)
- the dynamics of the gas-liquid interface (i.e. bubble coalescence and break-up, free surfaces etc.)
- and the modulation of turbulence due to the presence of two phases (in case of a continuous liquid phase the enhancement or damping of the liquid turbulence due to the presence of gas bubbles).

The new quality compared to 1D thermal hydraulics consists in the fact, that this empirics is geometry independent. The closure laws have to be formulated for the calculation cell, and no more for a specific component with a particular geometry, like T-junctions, valves, fuel rod bundles, pumps etc.. Beside the fact, that specific instrumentation is necessary to access to such microscopic processes, this has also a consequences for the strategy of experiments. It is no more necessary to keep strict

geometric similarity to plant components of interest, since the mesh generation allows a flexible adaptation of the geometry. Therefore, the design of experiments can be much more oriented at the phenomena to be studied. More attention can be paid to the specifics of available instrumentation during the planning of the experimental set-up with the goal to optimise the utilizable output. It is of course a necessary condition, that the phenomena to be studied are present in the experiment, but more freedom in choosing experiment geometry and scenarios can help to provoke the interesting phenomena in a more pronounced and selective way. This will be demonstrated at the example of experiments with a gas-liquid flow, which were carried out in a vertical pipe, using a movable, half-moon shaped diaphragm to introduce a strong disturbance into the flow. Despite of the fact, that this is a quite untypical geometry from the point of view of power plant design, the tests are very valuable for CFD validation in complex geometries.

2. Wire-mesh sensors

Function and construction of wire-mesh sensors are described in [1]. The sensor is sensible to the electrical conductivity of the fluid. In case of a two-phase flow, the water phase is slightly conducting, while the gas phase is practically an ideal insulator. Even small conductivities of the liquid (e.g. desalinated water) are sufficient for the measurement. The sensor consists of two grids of parallel wires which span over the measuring cross section. The wires of both planes cross under a certain angle, preferably 90 deg. During the signal acquisition, one plane of electrode wires is used as transmitter, the other as receiver plane. The transmitter electrodes are activated by supplying them with voltage pulses in a successive order. The current at a receiver wire resulting from the activation of a given transmitter wire is a measure of the conductivity of the fluid in the corresponding control volume close to the crossing point of the two wires. The currents from all receiver wires are sampled simultaneously. This procedure is repeated for all transmitter electrodes. After activating the last transmitter wire, a complete matrix of measured values is stored in the computer, which represents the complete two-dimensional conductivity distribution in the sensor cross section at the time of measurement.

The data evaluation starts from the transformation of the instantaneously measured electrical signals into local instantaneous gas fractions. At each measuring location the instantaneous conductivity signal is related to the signal characteristic for plain water. The result is a matrix of local instantaneous volumetric gas fractions. From this data, cross-section averaged gas fractions as well as radial gas fraction profiles can be calculated [2]. The accuracy of the gas fraction measurement is discussed in [3]. Three different methods are available to visualize the resulting gas fraction data: (1) instantaneous gas fraction distributions in the measuring plane, (2) virtual sectional side views and (3) virtual side projections [4].

Radial gas velocity profiles were obtained by means of a point-to-point cross-correlation between the signals of both sensors placed in a certain distance behind each other [4]. An alternative is a time-of-flight analysis of the bubbles crossing both successive measuring planes [5].

Bubble size distributions are gained using the algorithm described by [6]. First step is an identification of bubbles. A bubble is defined as a region of connected gas-containing elements in gas fraction data that is completely surrounded by elements containing the liquid phase. Each element of such a region obtains a common number that is unique for the detected bubble, a so-called bubble identificator. Local instantaneous gas fractions adopt intermediate values between 100 % (gas) and 0 % (liquid), when the corresponding control volume formed by a pair of crossing wires contains both gas and liquid in the same time. Furthermore, signal noise may also lead to such intermediate values. Consequently, a sharp definition for elements filled with gas cannot be given and the introduction of a threshold is inevitable. An optimisation of this procedure is described in [6], where a so-called differential threshold was introduced.

After the bubble identification, the volume of the bubble is obtained by integrating the local gas fraction over elements owning the given bubble number. The sum of gas fractions is multiplied by the

extension of the control volume, which is the product of the lateral electrode pitch in x and y directions and the sampling period multiplied by the bubble velocity. Often individual velocities of bubbles are not known. In these cases, the time-averaged gas phase velocity taken from the radial velocity profile at the radial position of the centre of mass of the given bubble is taken as an approximation. A very powerful technique to analyse the evolution of the flow structure is the calculation of radial gas fraction profiles decomposed according to bubble size classes [2].

If only one single sensor is available, the diameter of the bubbles within the measuring plane can be taken as a substitute. It is derived from the maximum part of the area of the measuring cross-section covered by the given bubble during its passage. For studies of the structure of the bubble-size distribution, the resulting distributions of the lateral diameter is a useful substitute, although it is not exactly equal to the equivalent bubble diameter, but has the advantage that it it can be derived without knowledge of the velocity.

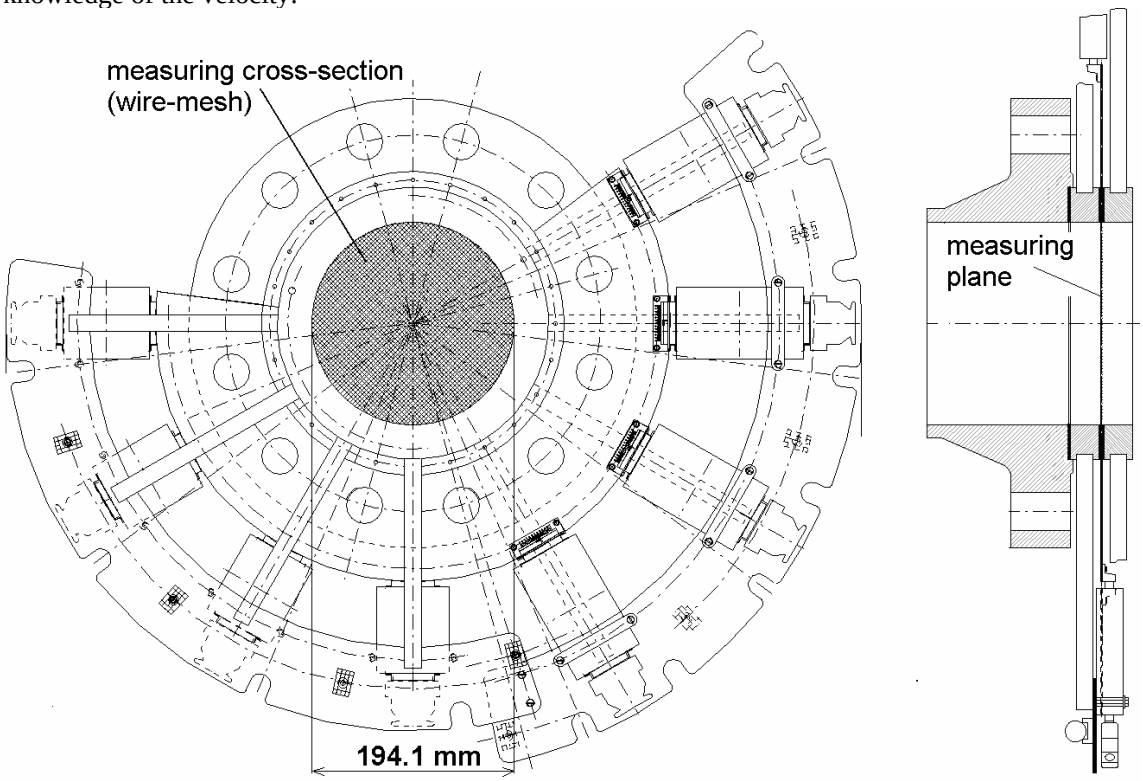

Fig. 1 Wire-mesh sensor for an air-liquid flow at atmospheric pressure and ambient temperature, 64x64 measuring positions, lateral resolution 3 mm, time resolution 2500 frames per second

Mesh sensors are available for a wide range of operation conditions. The biggest sensors for two-phase flow studies being in use cover a cross-section of a pipe of 200 mm nominal diameter with a network of 64 x 64 measuring positions in a stepwidth of 3 mm. These sensors are available for experiments with an air-water flow (Fig. 1) at atmospheric pressure and ambient temperature, but also for steam-water tests at 70 bar and the corresponding saturation temperature of 286 °C, [7] (Fig. 2). Special sensors were developed for water hammer experiments in the frame of the WAHALoads EU project [8]. They are equipped with reinforced electrode rods with a lentil-shaped cross-section in order to withstand the high loads during the pressure surges. Micro-thermocouples of 250 µm diameter are inserted into these electrodes (Fig. 3). They supply information about local instantaneous temperatures, which can be directly correlated with the void detection. This allows to measure the thermal non-equilibrium during the cavitational water hammers.

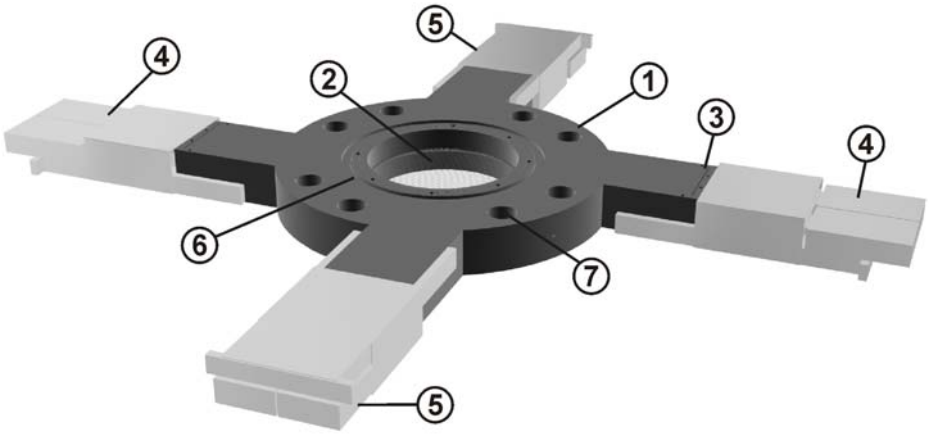

Fig. 2 CAD image of the complete sensor for a 195 mm inner diameter pipe, 64x64 electrodes [7]
1 - sensor body, 2 - measuring plane with wires, 3 - location of sealed bushings ("ear"), 4 - driver unit, 5 - receiver pre-amplifier, 6 - cover ring, 7 - bolt hole of flange connection

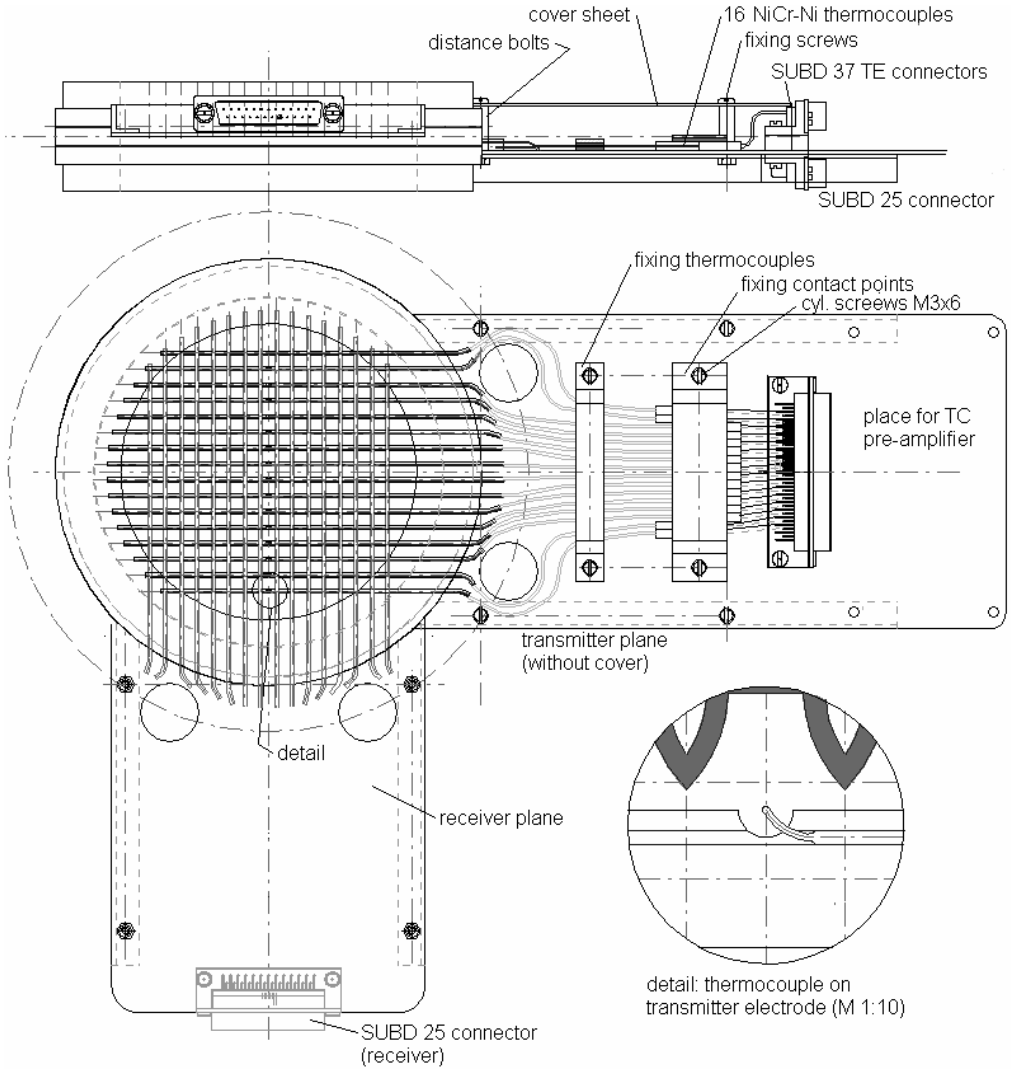

Fig.3 Mesh-sensor DN100 with 2x16 electrode rods and 16 micro-thermocouples for cavitational water hammer tests in the frame of the WAHALoads EU project

3. Single-phase mixing experiments

Mesh sensors are very much suitable for single-phase mixing studies, when different qualities of the liquid portions to be mixed cause a difference in the electrical conductivity. In model experiments, a fluid stream can be labelled by adding small concentrations of salts that increase the conductivity. Optional, other additives that do not affect conductivity (too much) can be used to simulate gradients of other physical properties, like density or viscosity. The wire-mesh electronics deliver measuring values that are linearly dependent from the local conductivity. At low concentrations of the tracer salt, the latter depends from the concentration of the salt in a linear way, too. If calibration values, i.e. measuring values for both miscible fluids, are known, a dimensionless mixing scalar reflecting the relative local concentration of the labelled fluid in the unlabelled one can be directly expressed from the measuring values by relating it to these calibration values.

A quite successful application of this technique consists in the ROCOM tests dedicated to coolant mixing problems in pressurised water reactors. A summary about the test facility and the achieved results can be found in [9] and [10]. There is a comprehensive presentation on this conference about the latest results obtained at ROCOM [11].

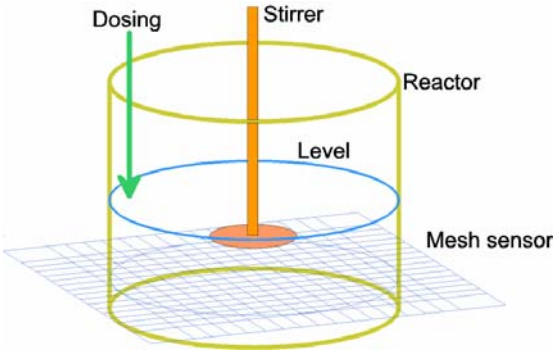

Fig. 4 Model Stirred of a stirred vessel reactor with a wire-mesh sensor (16x16) for mixing studies, resolution ~16 mm

Another application that is suitable to demonstrate the merits of mesh sensors are mixing studies in stirred tanks. Fig. 4 shows a test performed at the University of Erlangen, where a flat plate stirrer was installed in a cylindrical vessel. A mesh sensor of 16 x 16 crossing points was installed to cover the full horizontal cross-section plane below the stirrer. The tank was filled with desalinated water. To start the transient, a small quantity of salt water was poured into the tank at its periphery. The obtained data shows the mixing process in very detail. If the mixing scalar, i.e. the dimensionless concentration, is plotted as a function of time for all available measuring points, the process of the homogenisation is very well reflected. The so-called mixing time, which is the time after that the inhomogeneity has dropped below a predefined threshold (e.g. ±5 % or similar) can be determined with much higher reliability that in case of the traditional use of a local concentration measurement. As shown in Fig. 5, the mesh sensor beside this reveals details of the mixing process, like the stirrer-induced rotation of the tracer cloud. Furthermore, fluctuations of the local mixing scalar can be measured.

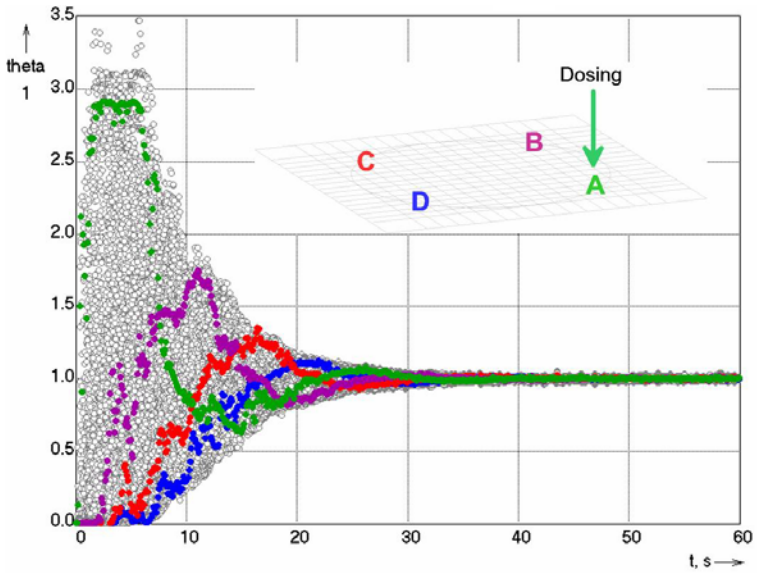

Fig. 5 Dimensionless concentration (mixing scalar) as a function of time for all available measuring points of the mesh sensor during the stirred vessel experiment (selected points highlighted by colour)

A more sophisticated experiment in a similar configuration was a mixing test with gas injection, which refers to the stirring of a steel melt [12]. For this, an air injection nozzle was installed in the bottom of the vessel. The mesh (16 x 16) was refined in the centre of the measuring plane to a lateral pitch of the electrode wires of 4 mm in order to resolve the gas bubbles, too. Tracer was added at the periphery when the gas supply was operating. The signal of the sensor shows short break-downs of the conductivity each time a bubble crosses the measuring plane. Conductivity changes due to the mixing of the tracer have a much lower characteristic frequency. This allowed to separate both signal components, as shown in Fig. 6 for the time history of the signal at a selected crossing point in the centre of the sensor matrix. This allowed to characterise the tracer distribution and the gas bubbles simultaneously (Fig. 7).

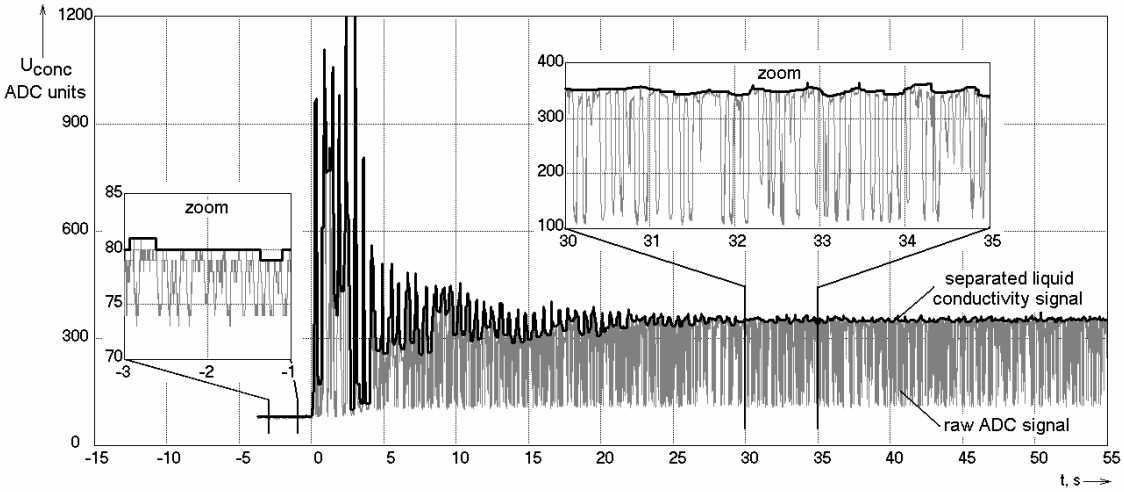

Fig. 6 Signal separation into a bubble and a tracer component, measuring point i=8, j=8 of the sensor matrix, experiment with tracer addition, air flow rate: 1.6 Nm³/h [12]

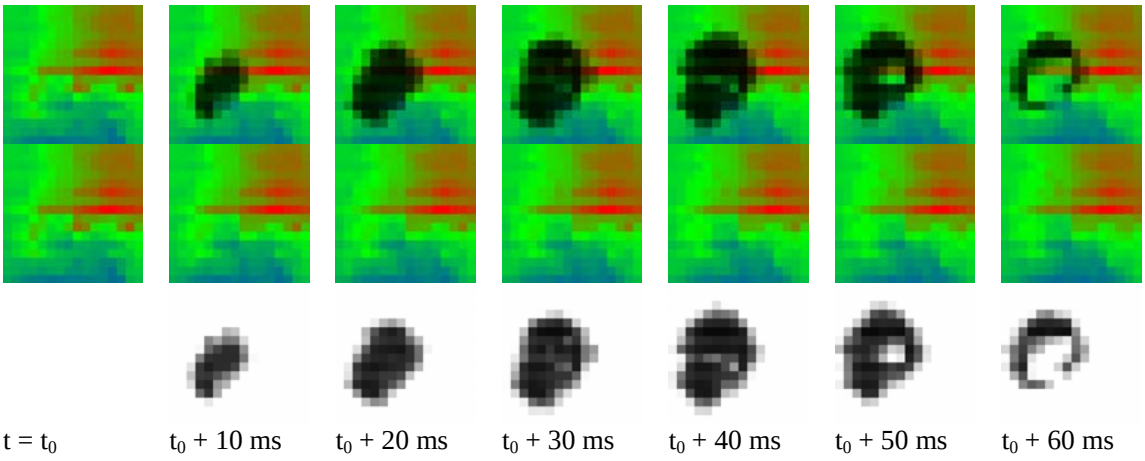

Fig. 7 Decomposition of tracer distribution and local instantaneous void fraction during the passage of a single bubble in the bubble induced mixing test of [12], upper row: concentration superposed with void fraction, middle row: concentration, lower row: void fraction

This demonstrates that a bubble signal and conductivity fluctuations of the liquid phase can be separated by adequate signal processing. This in fact can be used to perform a combined velocity measurement for the gaseous and the liquid phase together. In general, the gas velocity is assessed by evaluating the time of flight of bubbles or by cross-correlation techniques between two successive mesh sensors (or, respectively, between the measuring planes of a three-layer sensor). This method can be extended to the liquid phase, if conductivity fluctuations are present. In case of necessity, such fluctuations can be generated by a tracer injection, which can also be pulsed.

4. Evolution of a gas-liquid two-phase flow in a vertical pipe

Vertical pipe flow is nearly optimal for the derivation of geometry-independent closure relations for forces acting at bubbles as well as for bubble coalescence and fragmentation rates, because the gas phase travels together with the liquid flow within a relatively stable velocity profile and can be observed over a comparatively long time. Bubble forces are reflected by the evolution of the gas fraction profiles, while the change of the bubble size distribution along the flow path contains information about coalescence and break-up frequencies.

To that end the so-called "variable gas injection system" at the TOPFLOW facility was constructed [13]. It is a 9 m tall vertical pipe of 200 mm nominal diameter, which is equipped with gas injection units at six different heights. Each unit has three annular distributing chambers, from which gas or steam enters the test section via a number of orifices in the pipe wall (Fig. 8). In order to avoid an obstruction of the cross-section by the gas injection device for the flow coming from another gas injection port located upstream, preference was given to wall orifices against other spargers that would occupy part of the cross-section. For studies of the non-drag forces, this has a certain advantage, since the gas is forced to perform a radial motion towards the centre of the pipe. The changes of the radial profile along the pipe are therefore a sensible indicator for the absolute magnitude of the non-drag forces (Fig. 9).

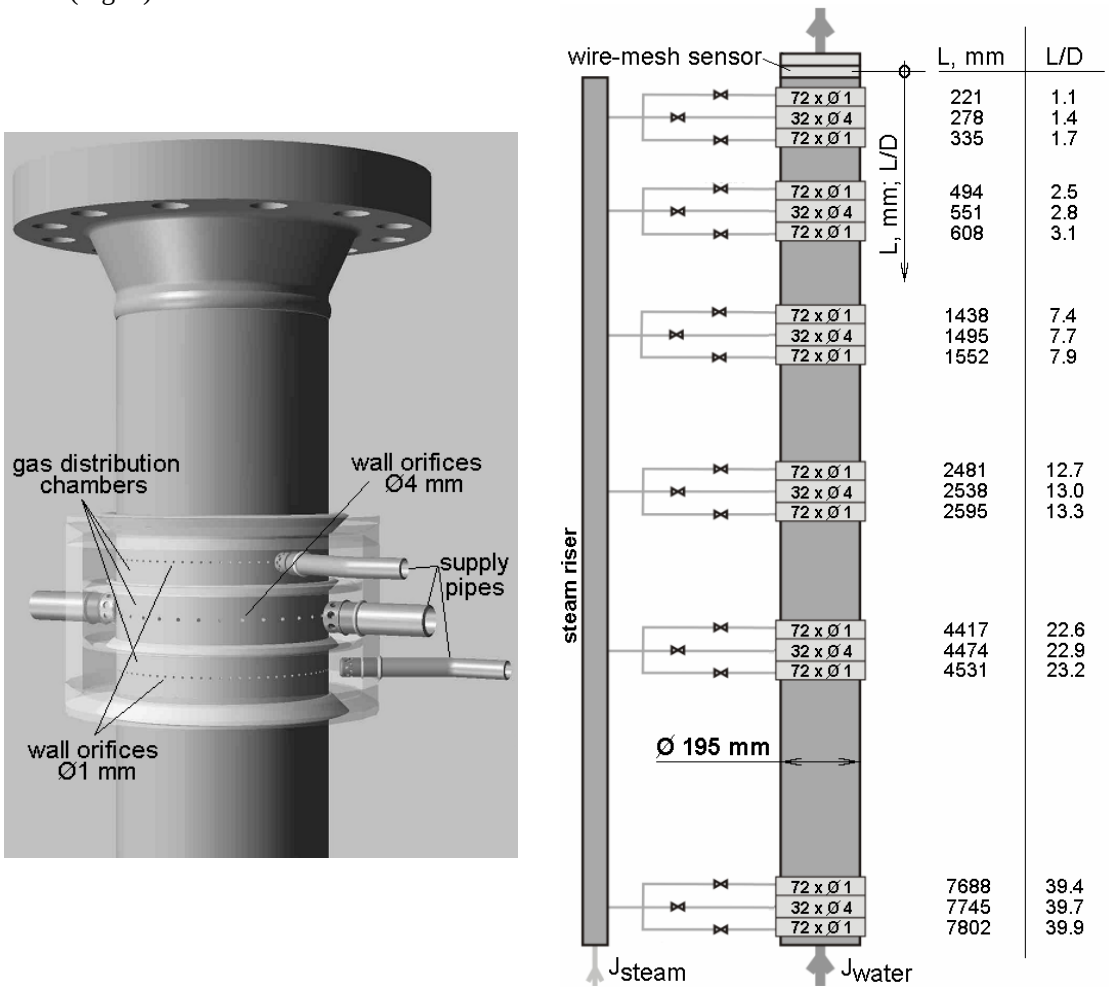

Fig. 8 Vertical test section of TOPFLOW with variable gas injection for studying the evolution of the flow structure in a large pipe of 195 mm inner diameter

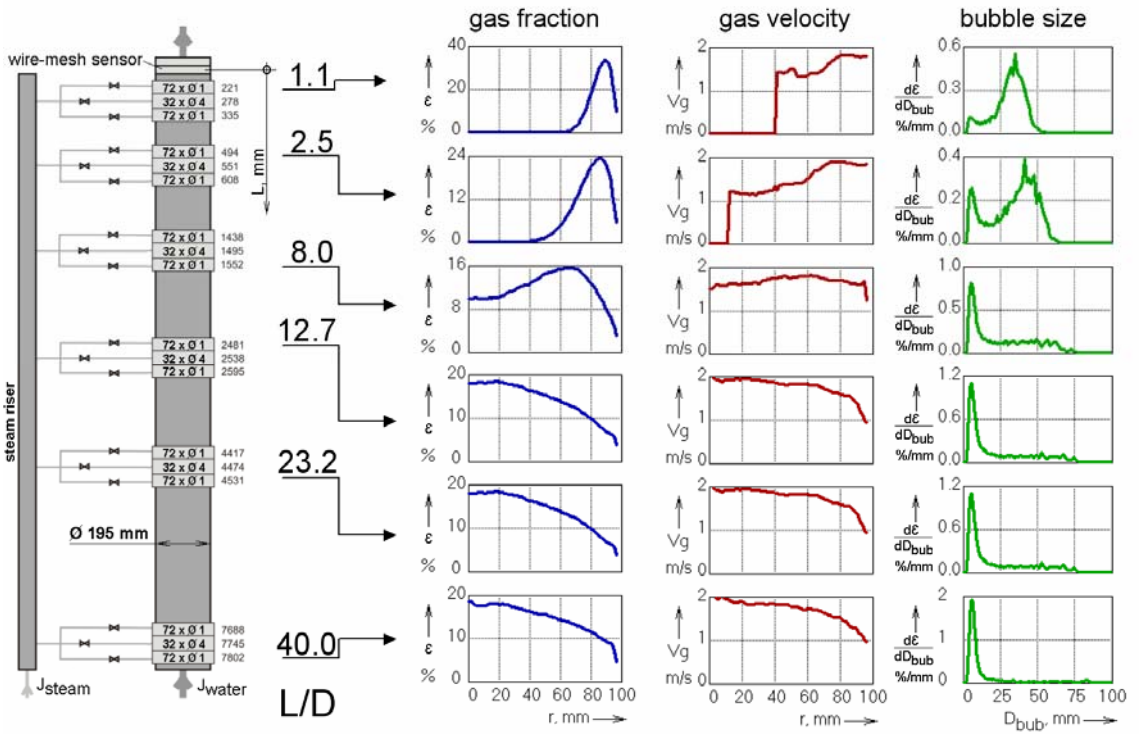

Fig. 9 Gas fraction and gas velocity profiles as well as bubble size distributions in the test pipe DN200 in an air-water experiment at J_L = 1 m/s and J_G = 0.22 m/s, T = 30 °C, p = 0.12 MPa at sensor position, gas injection orifices: D_{inj} = 1 mm [13]

It is an important strength of the wire-mesh sensors that the bubble recognition capability can be used to extract radial gas fraction profiles that are decomposed into bubble-size classes. This technique reveals the lateral movement of the bubbles as a function of the bubble size. As shown in Fig. 10, the result of the lift force inverse according to Tomiyama [14] can be studied in a polydisperse bubbly flow (compare [13]). Small bubbles still form a wall peak, even when the total gas fraction profile has a central peak. Data of this kind is the basis for the validation of the interfacial momentum exchange in a multi-bubble class approach used in the Inhomogeneous MUSIG model of CFX-10 [15].

The vertical test section is designed for an operation at 7 MPa and the corresponding saturation temperature, which allows to carry out both air-water and steam-water tests under identical boundary conditions. In tests at 6.5 MPa and 280 °C it was demonstrated that the critical bubble diameter of the change of the direction of the lift force decreases with growing pressure (Fig. 11). This confirms the correlation of the effect with the Eötvös number, since the decrease of the surface tension with growing saturation temperature results in a decrease of the critical bubble diameter arising from the assumption of a constant critical Eötvös number.

Another important issue is the correct modelling of bubble coalescence and fragmentation. Here, the capability of the sensor to deliver bubble-size profiles is crucial. It allows a very sensitive adjustment of model parameters in the corresponding model equations. Remember that the change of bubble size distributions can be separated from the different behaviour of the bubbles concerning their lateral displacement. A selected result is given in Fig. 12. As shown there, bubble-size distributions converge to an equilibrium profile much faster at high parameters. Furthermore, the air-water flow at low parameters tends to form very large bubbles at much lower superficial gas velocities than the steam-water flow at 6.5 MPa, while the peak of the small bubbles is much wider in case of the high pressure tests.

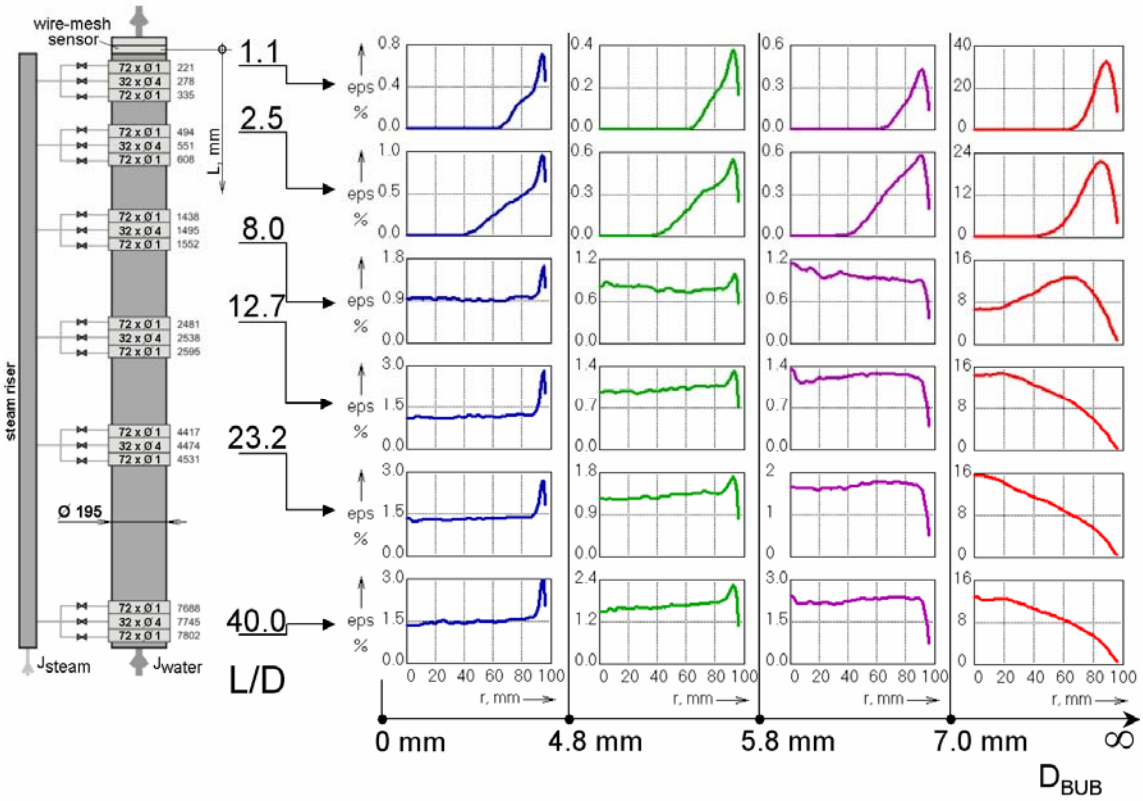

Fig. 10 Gas fraction profiles decomposed according to bubble size classes in the test pipe DN200 in an air-water experiment at J_L = 1 m/s and J_G = 0.22 m/s, T = 30 °C, p = 0.12 MPa at sensor position, gas injection orifices: D_{inj} = 1 mm [13]

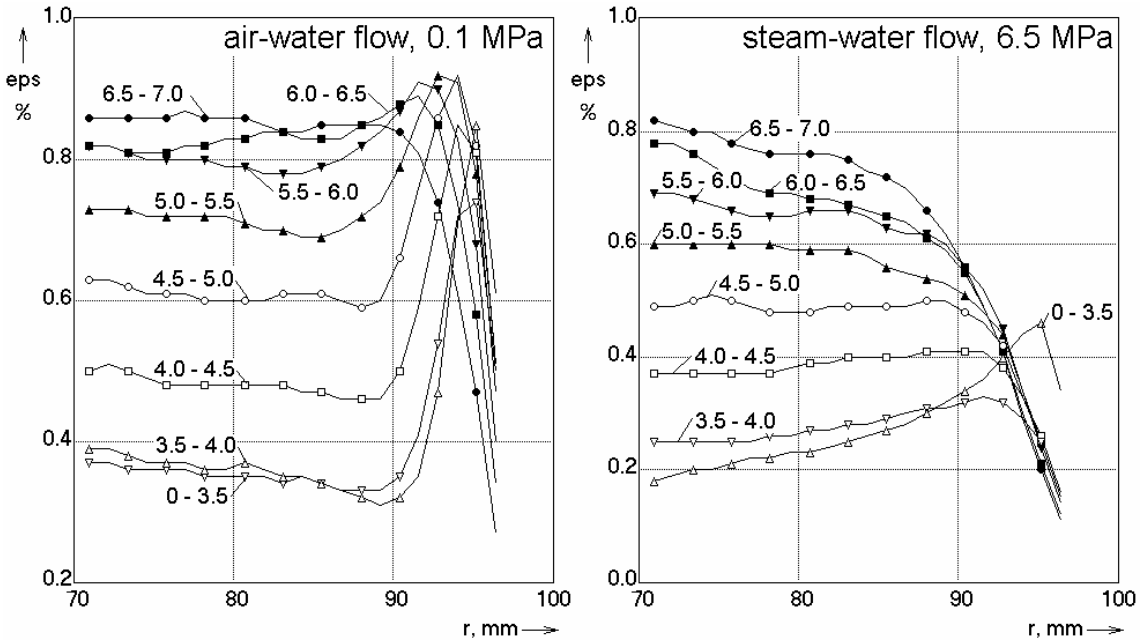

Fig. 11 Gas fraction profiles decomposed according to bubble size classes in the test pipe DN200 at J_L = 1 m/s and **J_G = 0.22 m/s**, L/D = 40, gas injection orifices: D_{inj} = 4 mm [13]

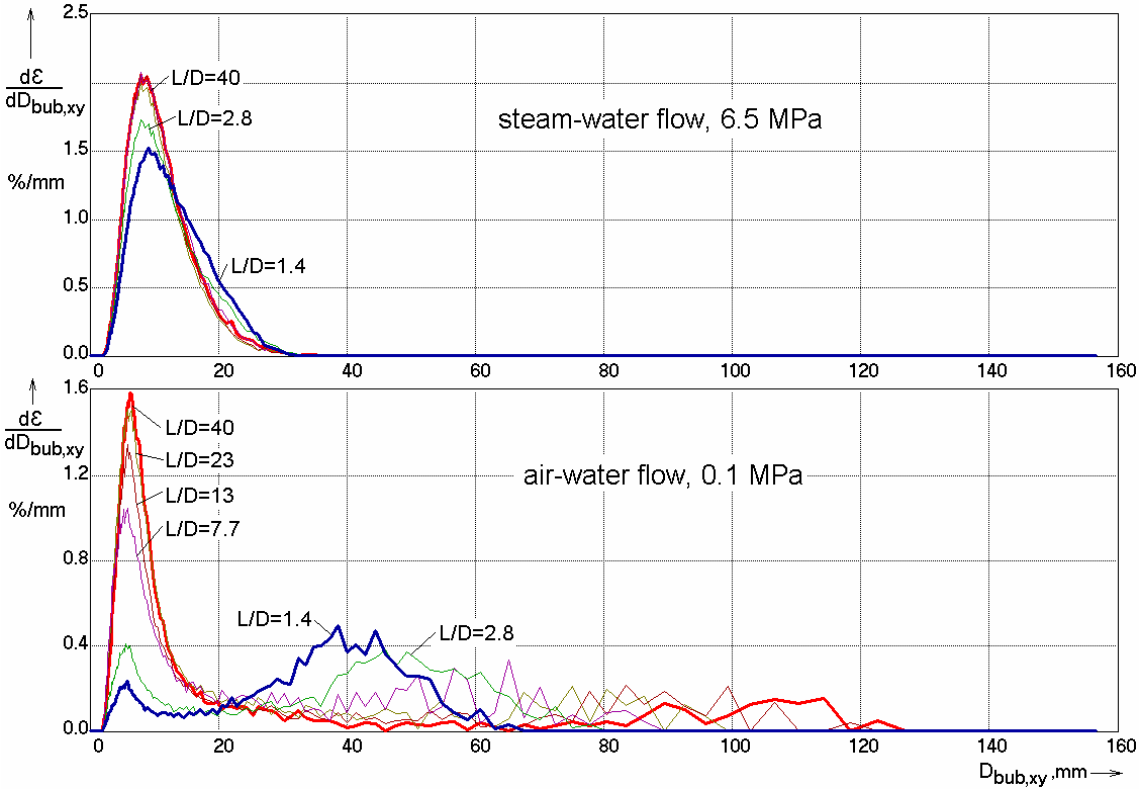

Fig. 12 Gas fraction profiles decomposed according to bubble size classes in the test pipe DN200 at J_L = 1 m/s and $\mathbf{J_G = 0.22\ m/s}$, gas injection orifices: D_{inj} = 4 mm [13]

5. Turbulent dispersion in a gas-liquid flow

The fact, that a pair of successive wire-mesh sensors was available, was widely used to correlate their signals in order to obtain profiles of the gas phase velocity (see Fig. 9). Time series of recorded at the crossing points that are at identical position within the measuring planes of both sensors are cross-correlated. The position of the maximum of the cross-correlation function corresponds to the average travelling time of bubbles from the first to the second sensor. By dividing the known distance between the sensors by the delay time, a local gas phase velocity is gained.

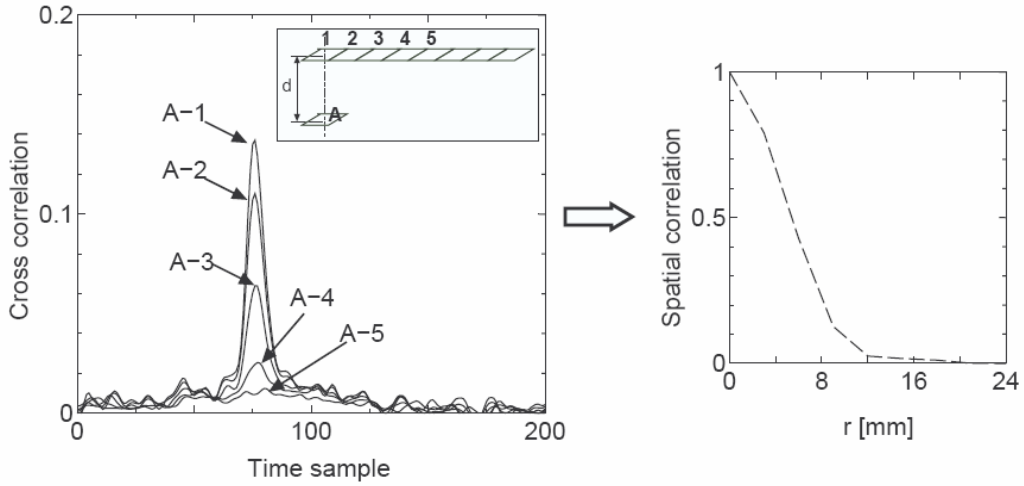

Fig. 13 Cross-correlation with an additional lateral shift between to successive wire-mesh sensors, left: time dependent cross-correlation functions, right: decrease of maximum with growing lateral shift [16]

The cross-correlation calculated for two positions at a certain axial distance that is kept constant decreases with growing lateral shift. It finally vanishes completely, when a position in the second sensor is reached, which is not accessible for bubbles that crossed the fixed position in the first sensor. In the central region of the pipe, turbulent dispersion dominates over other non-drag forces. The width of the spatial correlation therefore characterises the statistical movement of the bubbles in lateral direction caused by turbulence. Since bubbles have a finite size, a cross-correlation of the signals coming from a fixed crossing point in the first sensor and a second, laterally shifted point in the same sensor has also a finite width, which characterizes the average bubble size (ACF in Fig. 14). This effect is superposed to the action of the turbulence, which can be separated by deconvoluting the CCF with the ACF, i.e. by seeking a transfer function that converts ACF into CCF. For this, a Gaussean distribution of the transfer function was assumed and the dispersion vas varied to match the measured CCF by a convolution of ACF and transfer function. The width of the Gaussean transfer function contains the information about the turbulent diffusion (Fig. 14).

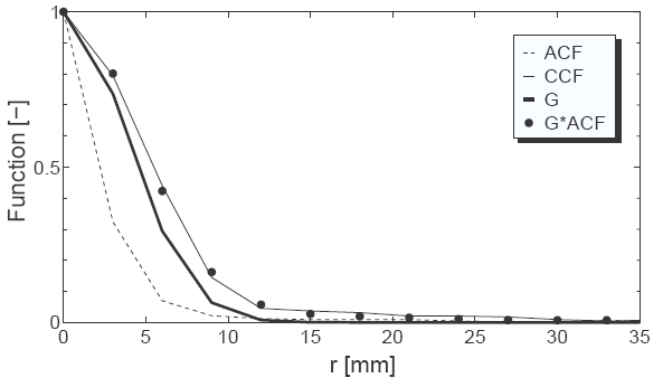

Fig. 14 Example for spatial cross (CCF) and auto (ACF) correlation functions, a result of a deconvolution (G) and a test convolution (G*ACF) to show the accuracy of the Gaussean fit [16]

It was found, that a turbulent enhancement takes place, that is well described by the algebraic equation of Sato [17, 18] even in the region of churn-turbulent flow, for which the Sato equation was not validated before (Fig. 15). Note, that Sato's equation may not be optimal for the application in CFD codes, that use transport equations for turbulence quantities, where the mentioned effects have rather to be reflected by additional source terms in the turbulence model. It was shown that a sharp increase of the turbulent diffusion observed at a certain superficial gas velocity corresponds to the appearance of very large bubbles in the flow [16].

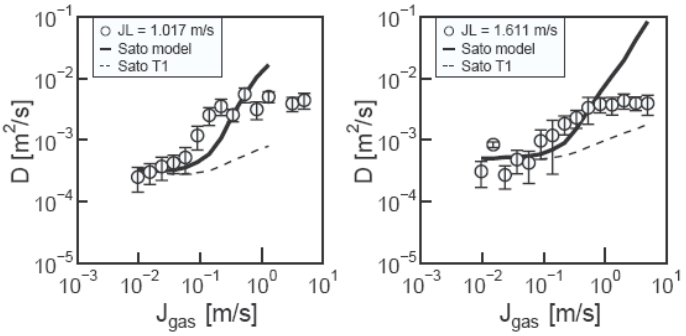

Fig. 15 Selected results of the turbulent diffusion coefficient as a function of the superficial air velocity, comparison to the Sato model [16]

6. Condensation due to liquid sub-cooling

During steam-water operation it is possible to create thermal non-equilibrium in the large vertical test section of TOPFLOW. In a series of tests at 1 and 2 MPa, this was done by throttling the outlet of the test section downstream of the mesh sensor by partially closing a ball valve. Pressure drops between 70 and 160 kPa were impeded, a sub-cooling of up to 5 K was reached. The throttling causes the liquid in the test section to be sub-cooled because the pressure is increased above saturation pressure. Consequently, steam injected into the pipe condenses due to interfacial heat transfer. This process was observed by the wire-mesh sensor and by varying the distance between steam injection and measuring position using the variable gas injection system described above (Fig. 8).

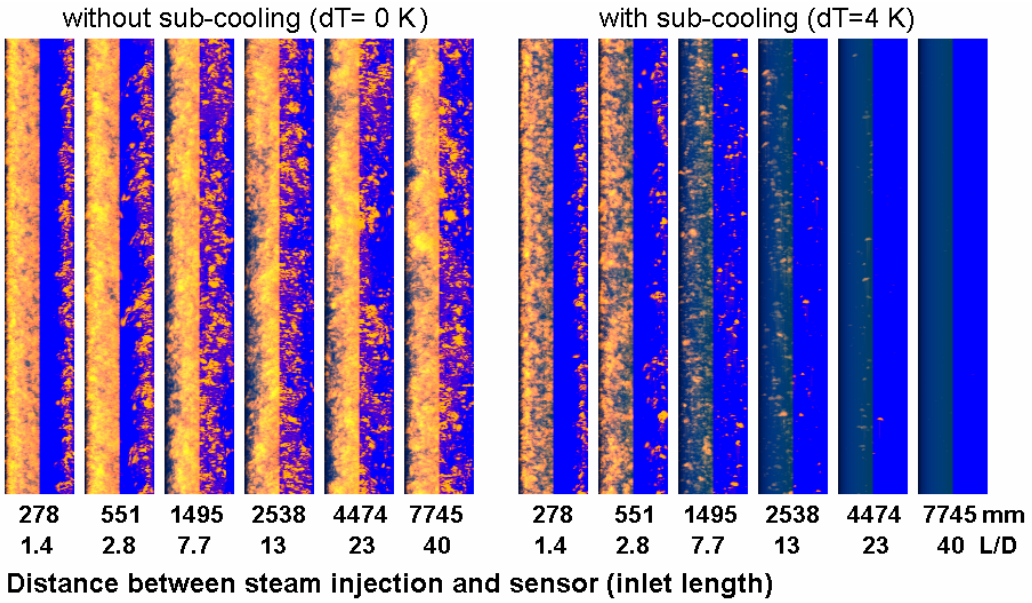

Fig. 16 Steam-water test in the large TOPFLOW test pipe with and without subcooling of the liquid phase, virtual side projections (left halves of the columns) and side views of virtual central cuts (right halves) of the mesh sensor data, p = 2 MPa, J_L = 1m/s, J_G = 0.54 m/s, D_{inj} = 4 mm

The results show the typical phenomena observed in the tests without phase exchange (compare Fig. 9), like lateral bubble movement, coalescence and break-up, but superposed by the decrease of the bubble sizes due to condensation (Figs. 16 and 17). A reflection of the condensation process in the multi-bubble-class model requires the introduction of sink and source terms describing the transfer of bubbles from one class to another, smaller one due to the condensation. Such a model was composed by Lucas [19] using interfacial heat transfer correlations from the literature. It has shown to be able to predict the experimental results. It is ready for being implemented into multi-bubble-class CFD models.

Future activities are envisaged within the second stage of the TOPFLOW project, were it is planned to increase the sub-cooling by injecting cold water into the test section and to extend instrumentation.

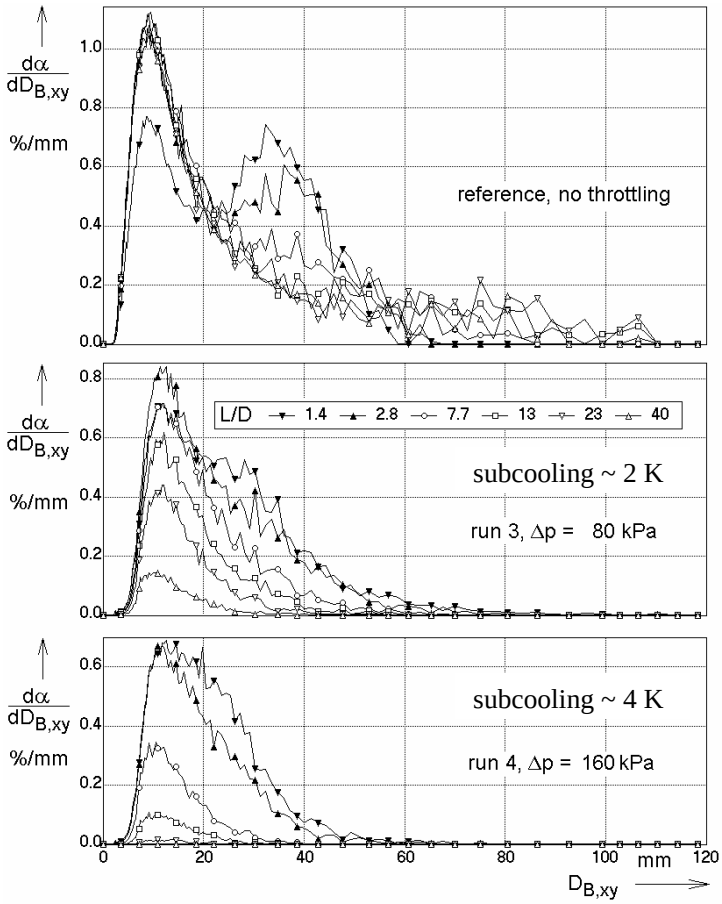

Fig. 17 Evolution of the bubble size distributions with and without condensation (parameters see Fig. 16)

7. Complex 3D two-phase flow fields

One of the test series at the large vertical test section was of TOPFLOW was dedicated to code validation in complex geometries. An obstacle was put into the pipe that obstructs nearly 50 % of the cross-section and creates a pronounced three-dimensional two-phase flow field. Curved stream lines, which form significant angles with the gravity vector, a recirculation zone in the wake and a flow separation at the edge of the obstacle are phenomena widespread in real industrial components and installations. Test series were performed with an air-water flow at ambient conditions as well as with a steam-water mixture at a saturation pressure of 6.5 MPa. Before the experiments were commissioned, an ANSYS CFX 10.0 pre-test calculation was carried out for one of the air-water tests [20].

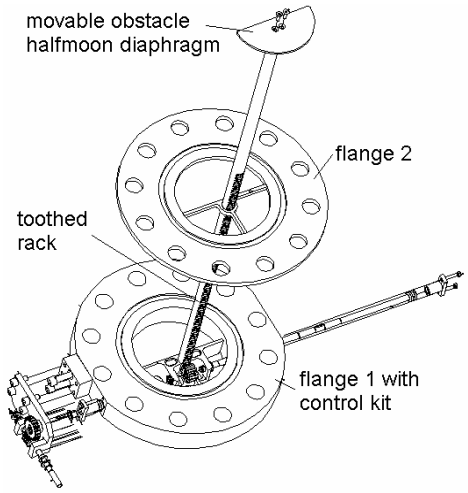

Fig. 18 Movable obstacle for the vertical test pipe DN200

The diaphragm (Fig. 18) is a half-moon shaped disk, the straight edge of which is arranged along the diameter of the pipe, while the circular edge is at a distance of 10 mm from the inner wall of the pipe. The disk is mounted on top of a toothed rod connected to a translation mechanism to change the axial position of the diaphragm. Both obstacle and moving mechanism can be inverted and mounted either upstream or downstream of the wire-mesh sensor. The described arrangement allowed acquiring local instantaneous void fractions from the full cross-section of the pipe within the three-dimensional flow field around the diaphragm. The distance between sensor and diaphragm was varied from 10 mm to a maximum distance of 520 mm without moving the sensor position, which is essential to perform high-pressure experiments in an efficient way, i.e. without dismantling and rearranging the test facility (Fig. 19) each time the measuring position has to be changed.

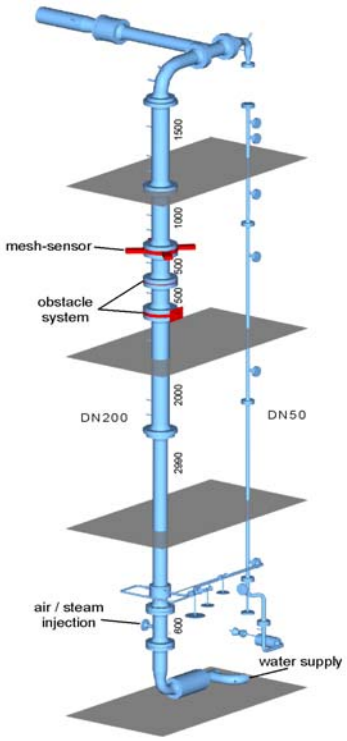

Fig. 19 Test section DN200 with sensor and obstacle

The sensor data was used to calculate two-dimensional time-averaged void fraction distributions in the measuring plane. By combining the information from different distances between sensor and diaphragm, full three-dimensional void distributions around the obstacle were obtained. A centre cut along the axis of the test pipe in a vertical plane perpendicular to the straight edge of the half-moon diaphragm is a very illustrative way to visualize the void fraction field. Beside void fractions, time-averaged local liquid velocities can be extracted by evaluating the transit time of bubbles of a certain range of diameters. The lateral extension of each individual bubble related to the transit time of a bubble is proportional to the bubble velocity. A local instantaneous value of the liquid velocity is available after subtracting the bubble rise velocity. The proportionality factor was found by integrating the liquid velocity and comparing the superficial water velocity reconstructed in this way with the injected liquid flow rate. Time-averaged profiles of the axial liquid velocity are calculated by averaging individual values from a manifold of analysed bubbles.

The void fraction and liquid velocity profiles for an air-water experiment with J_L = 1 m/s and J_G = 0.037 m/s are shown in

Fig. 20 together with the results of steady-state CFX-10 pre-test calculation. The latter was carried out using the two-fluid model with a mono-disperse bubble size of 5 mm and a two-equation turbulence model (SST) on a grid of 473000 hexahedral mesh elements. Calculation and experiment show the same global structures. There is a stagnation point in front of the diaphragm that is depleted from bubbles. Bubbles are pushed away from the stagnation point due to the curvature of the streamlines. The flow separates at the edge of the obstacle. Downstream, there is a stagnation zone with a recirculation area above the obstacle and a jet coming from the non-obstructed part of the cross-section. In the recirculation area, gas phase is accumulated. The local maximum of the velocity in the centre of this region corresponds to a downwards motion of the liquid phase. Negative velocities cannot be distinguished from positive one, since the measuring method described above is not sensible to the direction of the bubble passage through the measuring plane.

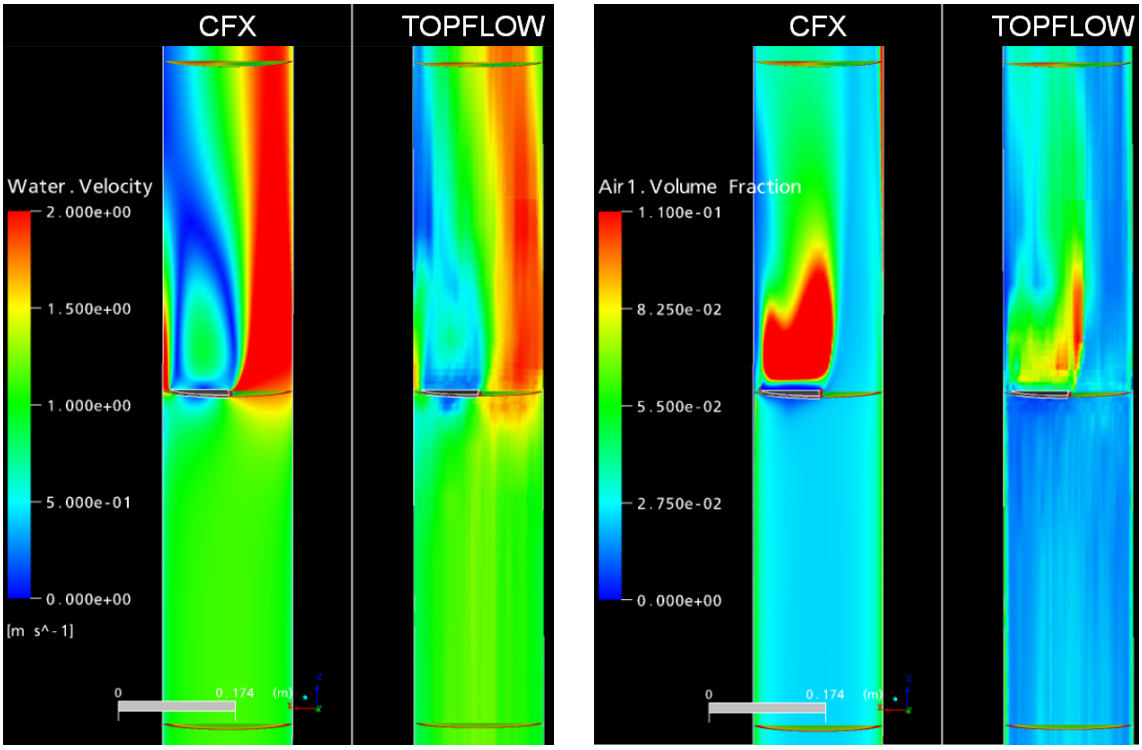

Fig. 20 Comparison between experiment and CFX pre-test calculation for absolute water velocities (left) and gas volume fraction distribution (right) for the region from 0.5 m upstream to 0.5 m downstream the obstacle; air-water test at J_L=1 m/s and J_G=0.037 m/s [20]

A significant deficiency of the pre-test calculation is the prediction of significantly higher void fractions. This is probably due to the assumption of mono-disperse bubbles with a too small size compared to the test. Here, improvements are expected with the application of the Inhomogeneous MUSIG model.

All phenomena occurring e.g. in an industrial safety valve are reflected in the test geometry (Fig. 21). There is a topologic similarity between both geometries, although the geometry itself is different. This illustrates that a code validation against data from such kind of experiments contributes to the solution of industrially relevant problems despite of the simplifications that enable a very comprehensive acquisition of experimental data.

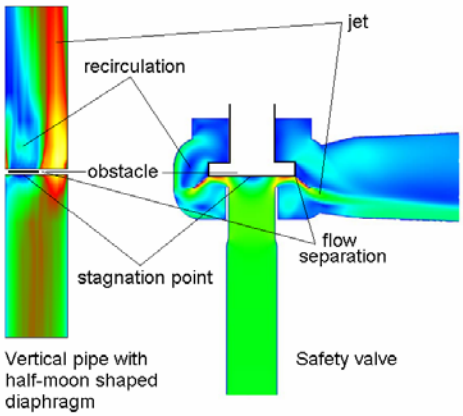

Fig. 21 Topologic similarity between the obstacle in the test pipe and an industrial safety valve

8. Gamma tomography

The attenuation of ionising radiation is used as a non-intrusive method to measure the average density of an object along the chord of the transmission. In case of a two-phase flow, this offers the possibility of a void fraction measurement. Distributions of density or void fraction can be obtained by tomography. Using a fan beam and a line of multiple detectors, a 1D radiographic projection of the absorption density in the measuring cross-section is recorded. Source and detector assembly have to be rotated around the object in order to obtain projections in a large number of directions. From such a full set of projections, the 2D distribution inside the object is reconstructed by means of analytic (filtered back projection) or algebraic image reconstruction methods. More sophisticated tomographs use cone beams and 2D detector arrays to record 2D projections, from which 3D distributions inside the object can be attained.

Since these gamma tomography set-ups have to rely on a mechanical rotation of quite bulky equipment around the object, the acquisition of a complete set of projections is slow. Consequently, this kind of tomography is restricted to steady-state flow conditions and can deliver only time averaged quantities. An example for the usefulness of such a slow gamma tomography is given by the recent upgrade of the fuel rod test facility KATHY of Areva NP [21] by a gamma tomography system of FZR [22, 23]. The detector arc consists of 320 LYSO scintillation crystals coupled to avalanche diodes with a lateral resolution of 2 mm. A fan beam comes from a Cs-137 source (662 keV) with an activity of about 7 Ci. The resolution is sufficient to quantify the time averaged void fraction in the sub-channels of the boiling water test bundle, which is a potential test case for CFD calculations.

It is clear that such systems cannot deliver 2D density distributions showing individual bubbles, like wire-mesh sensors do. For this, the imaging rate would have to be increased to at least more than 1 kHz. This is infeasible due to the mechanical rotation. Nevertheless, there is a way to observe fast transient processes in a two-phase flow, when the transient void fraction field changes periodically. In this case, the signal acquisition of the radiation detector assembly can be synchronised to the period of the changes in order to generate ensemble averaged projection data for short but periodically repeating time intervals.

This method was applied as a non-intrusive method to visualise the gas fraction distribution inside the rotating impeller of an axial pump delivering a two-phase flow [24]. The pump test facility is located at the Technical University of Dresden. Its impeller has three helical blades, the diameter is 220 mm. The pump operates at approximately 1500 revolutions per minute (25 Hz). Air-water mixture is used as model fluid, created by a gas distributor upstream the pump inlet nozzle. Later, the same technique was applied to a hydraulic coupling [25].

At 1500 rpm a complete set of projections must be obtained within time intervals of about 100 µs, if an angular resolution of 1 deg is required. Good image reconstruction requires about 10^2 projections. This is achieved by counting the pulses delivered by the detectors synchronised to the rotation of the impeller [24]. One revolution of the impeller is divided into a number of equal angular intervals. Each detector responsible for a given through-transmission chord is connected not only to one, but to a number of counter units via signal switches (Fig. 22). In this way, counter banks are organized, the number of which equals to the number of required angular intervals. Each counter bank corresponds to an angular interval of the impeller rotation. Signal switches (S) perform the successive connection of the detectors to the currently activated counters controlled by a clock signal of 10 kHz. Each counter is activated for the period of 100 µs.

The synchronisation of the signal acquisition is based on a trigger pulse generated at each revolution of the impeller. The arrival of the trigger pulse defines the zero angular position and forces the control unit to terminate the successive activation of the counters and to restart the counting process in the counters of the first bank. To achieve a sufficient statistical accuracy of the counting results, the measuring procedure is continued over a large number of pump revolution for 3 - 6 minutes.

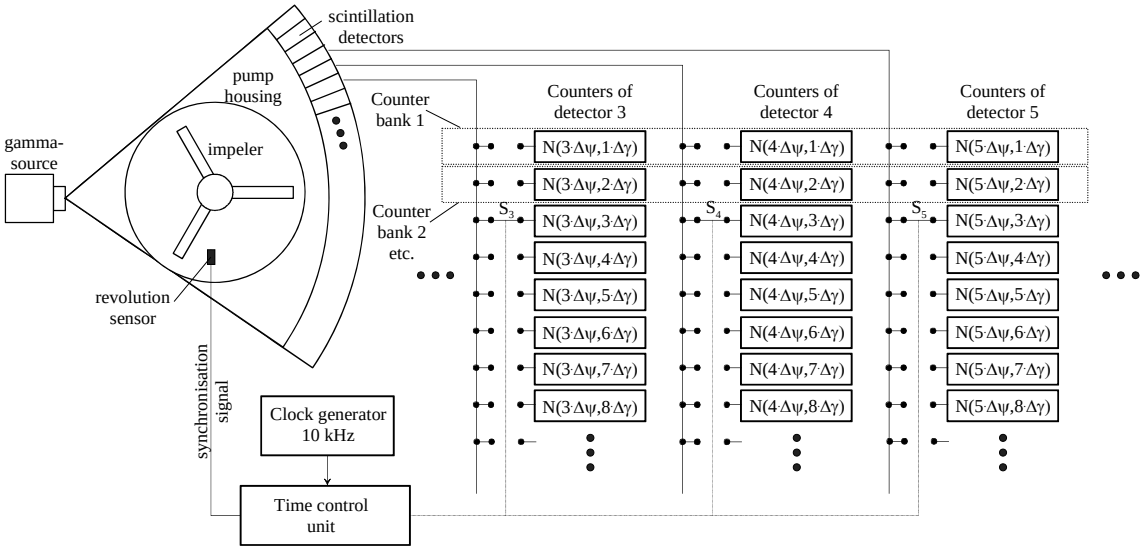

Fig. 22 Working principle of the time resolving gamma tomography for periodically changing void fraction fields

If a uniform or radial-symmetric distribution of the gas fraction at the inlet nozzle of the pump can be assumed, the gas fraction distribution inside the rotating parts of the pump is quasi-stationary related to the moving co-ordinate system due to symmetry. In this case the rotation of the gas fraction field itself can be used to obtain the necessary set of independent projections, while the tomography system can stand still. This situation is similar to the technique to rotate the object instead of the tomography system, but at very high revolutions.

The situation is different, if the gas fraction distribution at the inlet of the axial pump is depending from the azimuthal angle in the laboratory co-ordinate system. In this case the void fraction distribution cannot be regarded as quasi-stationary in the rotating co-ordinate system of the impeller. The only property which can be used is periodicity in time, i.e. it can be assumed that the void distributions found in identical intervals of the rotation angle of the impeller can be treated as quasi-stationary. To obtain the necessary projections for an imaging of this distribution, the tomography system must be rotated around the object, too. The image has to be reconstructed from a set of projections for one and the same interval of the impeller rotation angle obtained at the different aspect directions of the tomography system. In this way, for each interval of the impeller rotation angle an individual image can be reconstructed. The resulting series of images can be used for an animation of the periodically changing void fraction distribution inside the impeller.

For the measurements at the axial pump, a Cs-137 source with an activity of 185 GBq ($E\gamma$ = 662 keV, 5 Ci) is used. The source container is equipped with a fan-beam collimator. The detector arc consisted of 64 scintillation crystals of Bismuth-Germanate (BGO) with a front face of 10 x 10 mm² and a length of 30 mm. Photo-multipliers are coupled to the side planes of the crystals. The dimensions of the crystals correspond to a resolution of about 5 mm inside the measuring plane. The length of 30 mm is important for high quantum efficiency at the comparatively high gamma energy. This is a predecessor of the detector arc with 320 channels introduced before.

The void fraction distribution can be visualised only by means of differential tomography. For this purpose, a reference tomogramme is obtained for the case of plain liquid flow (Fig. 23). The distribution obtained after switching on the air supply is related to this reference case. The resulting tomographic image shows only those parts inside the measuring plane, where the gamma absorption density changed between the two working regimes, i.e. impeller and pump house structures disappear. The contours of these structures are overlaid to the tomographic images in Fig. 23.

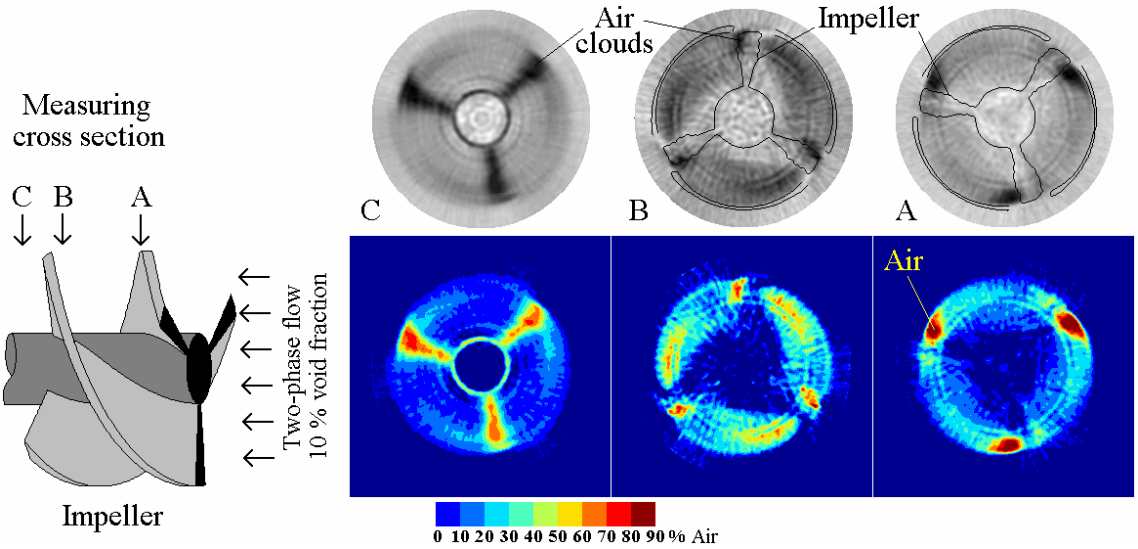

Fig. 23 Differential tomographic images of the void fraction distribution inside the impeller of the axial pump working in two-phase mode (average void fraction about 10 %)

The measurements were taken at different axial positions along the pump. In the measuring plane A, areas with air concentration are observed close to the back surface of the impeller blades. There is some evolution of the distribution in axial direction. Regions of increased void fraction are still observed in the wakes of the impeller blades (cross section C).

9. X-ray tomography

As outlined above, the framing rate obtained by tomography is defined by the maximum achievable revolution frequency of the rotating source-detector system and by the acquisition time necessary to achieve an adequate statistical reliability of the detector signals at a given activity of the source. The latter can be guaranteed by applying a source that is strong enough to produce a sufficient photon flux. Mechanical rotation reaches its limits at framing rates in the range of seconds. X-ray bremsstrahlung is produced when electrons hit a metallic target (often tungsten). Since electron beams can be switched and deflected, the mechanical rotation can be substituted either by a number of electronically controlled X-ray tubes that are placed around the object and activated in a successive order, or by deflecting the electron beam along a line on an otherwise extended target.

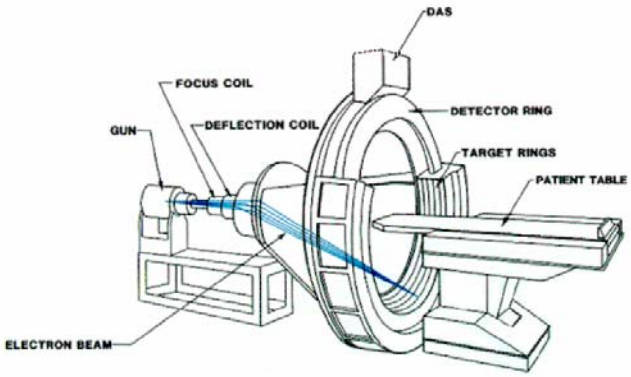

Fig. 24 Medical fast X-ray tomograph of Boyd & Lipton [26], generating up to 50 frames per second

Today there exist only a few tomographic devices which are able to produce fast sequences of cross-sectional images from an object. In medical diagnostics the electron beam tomograph (EBT) first introduced by Boyd & Lipton [26], is one example of such devices that use a scanned electron beam to produce X-ray computed tomography images with up to 50 frames per second - an image acquisition rate that is sufficient to investigate cardiovascular processes in human beings and animals (Fig. 24). However, although the EBT has brought completely new perspectives to medical

diagnostics, it is too slow for the investigation of two-phase flows, where frame rates of at least 1000 Hz are required, if individual bubbles have to be captured.

One device that has recently been built for studies on two-phase flows is the X-ray computed tomography apparatus introduced by Hori et al. [27]. It uses a circular arrangement of 60 pulsed X-ray tubes in combination with an annular X-ray detector slightly above the plane defined by the focal spots of the X-ray sources (Fig. 25). High-speed tomographic data acquisition is realised by repeated sequential flashing of all sources giving a frame rate of up to 2000 images per second. Beside the complexity and costs of this system there is also a compromise in axial resolution since the 360° tomography inevitably requires that the source and detector plane have an axial offset, clearly visible in Fig. 25. This in turn might cause problems to resolve small moving objects, such as particles or bubbles in a flow.

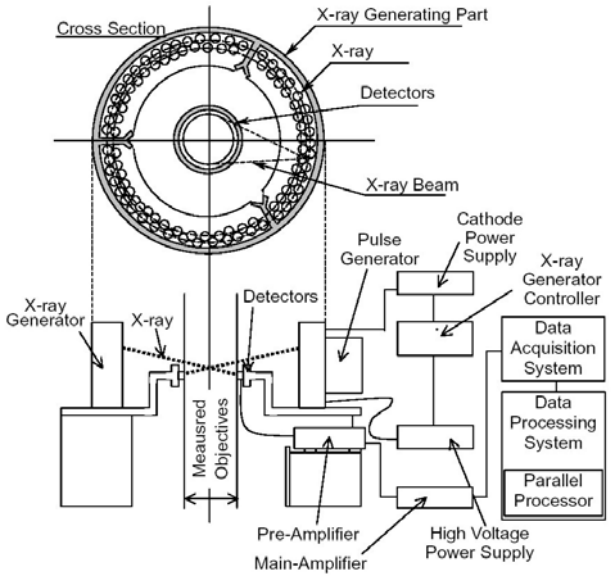

Fig. 25 Ultra-fast X-ray tomography system of Hori et al. [27] for fluid-dynamic experiments, imaging rate 2 kHz

Our own develoment [28] uses, contrary to the design in Fig. 25, a linear deflection pattern for the electron beam and a non-annular detector arc records transmission data of an object from different projection angles. This approach gives the highest achievable axial resolution and is comparatively moderate in effort and costs. For the inverse problem we applied iterative algebraic image reconstruction techniques to reconstruct the density distribution from a limited data set. The method has been experimentally tested on static and dynamic phantoms with a frame rate of 1000 images per second and a spatial resolution of approximately 1 mm in-plane and axial.

Fig. 26 shows the principal design of the computed tomography system with a scanned electron beam source. For the generation of the electron beam a conventional high power electron gun with up to 150 kV acceleration voltage and 600 mA continuous electron current has been used. The beam is vertically directed onto a cylindrical tungsten target whose axis is orientated perpendicular to the beam axis. The beam steering system comprises focusing and deflection coils together with high power, high speed coil current drivers. All components of this system have been especially designed and optimised for this tomography application. During a tomographic scan the electron beam is linearly deflected from its axial direction by applying a saw-tooth coil current pattern of 500 Hz frequency, thus producing a focal X-ray spot that moves forth and back between two turning points on a line segment on the surface of the tungsten target. The object is therefore scanned with a frequency of 1000 Hz.

The optimal X-ray detector geometry for tomography is an arc of contiguous sensor elements that surrounds the object up to the prolonged axis of the target. In that way all the detector pixels are exactly aligned in one plane with the focal spot path. For the initial experiments, however, we used a smaller detector with 64 elements. The detector elements are CdZnTe semiconductor pixels of 1.5 mm x 1.5 mm active area, 1 mm depth and 1.6 mm pitch. The detector electronics, which is physically separated from the pixel array, comprises 64 two-stage transimpedance amplifiers with 50 kHz bandwidth, followed by 12-bit analog-to-digital converters which sample the signals at 100 kHz in parallel and in synchronization with the beam deflection signal.

The first experiments were carried out in a vacuum box. A dynamic phantom was used that is shown in Fig. 27, left side. It consists of a DC motor driven rotating disk within an aluminium housing (cup) of 1 mm wall thickness and 40 mm outer diameter which can be filled with particles. Two steel pins are fixed on the disk in order to force the particles to irregular movements by bouncing. Two other steel pins that descend from the cover of the cup prevent the particles from moving only along a circumferential path. As test particles, small glass pearls from a necklace were used, which are of 4.5 mm diameter and possess through-holes of 1 mm diameter. With the detector array, this time arranged in a closer position to the object, the irregular movement of the pearls was recorded during a period of 0.8 s with a frame rate of 1000 images per second.

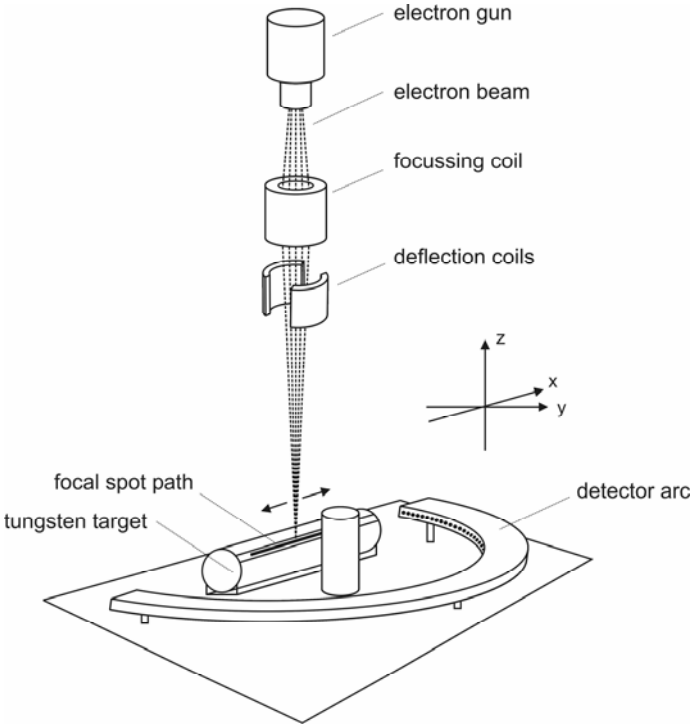

Fig. 26 Setup for a fast X-ray CT with a scanned electron beam source

Fig. 27 right shows single images of such a sequences for one, three, and ten pearls in the cup. The reconstruction algorithm in this case was MART. It can clearly be seen, that also the through-holes in the pearls can be resolved when they appear within the imaged plane. This indicates, that we achieve an axial resolution of at least 1 mm. The wall of the cup and the rotating steel pins are also reconstructed.

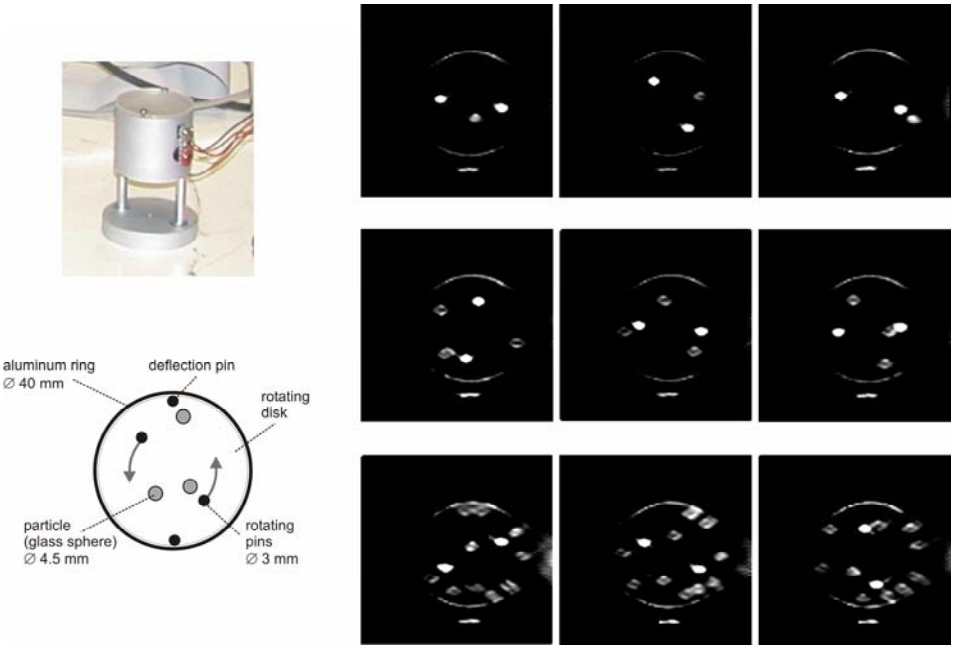

Fig. 27 Reconstruction results for a dynamic particle phantom. Left: photo and geometry of the phantom, right: images for the scenario with one (top), three (middle) and ten (bottom) particles

Summarising it was concluded that a fast X-ray computed tomography technique with a scanned electron beam source may have a high potential in imaging of transient density changes, especially in two-phase flow problems. In the meanwhile, the detector assembly was extended to 512 CdZnTe detectors. A dedicated electron beam source with a 2D deflection system was acquired, which is presently being put into operation for use in the TOPFLOW-II project. It is planned to install it on a new test section of 50 mm inner diameter, made from Titanium. We expect to obtain data from an upwards and a downwards steam-water flow at up-to 7 MPa with a resolution better than that of wire-mesh sensors and without the intrusivity of these devices.

The small diameter is a compromise that has to be taken because of the strong attenuation of the X-rays in larger steel pipes. Therefore, experiments at the large TOPFLOW test section (DN200) remain still a domain of wire-mesh sensors. An application of electron beam tomography would requite beam energies that can be achieved only by small accelerators, which demand major investments.

10. Neutron radiography

Neutrons have a number of advantages in terms of their attenuation in matter in comparison to photons, when a fluid consisting of light elements, like water, is to be studied. In this case, The attenuation is mainly due to either moderation, when the imaging is performed with fast neutrons, or due to absorption, but also scattering the neutrons out of their linear trajectory. Applications of neutron radiography known from literature are focussed on the use of thermal neutrons. As shown in Fig. 28, neutron attenuation allows to get contrast from nuclides different from those that are seen by high-energy photons. The most important feature is the sensibility to hydrogen, which is mainly due to the high cross-section of the elastic scattering, while heavier elements are less contributing to the contrast (see Fig. 29). As a consequence, the method is well suitable to sense water in ducts with metallic walls. The fact that boron is a very strong absorber makes it a good tracer for mixing studies. One can also think about combining photons with neutrons to create a composition-dependent contrast for distinguishing different fluid components, e.g. a boron tracer and bubbles.

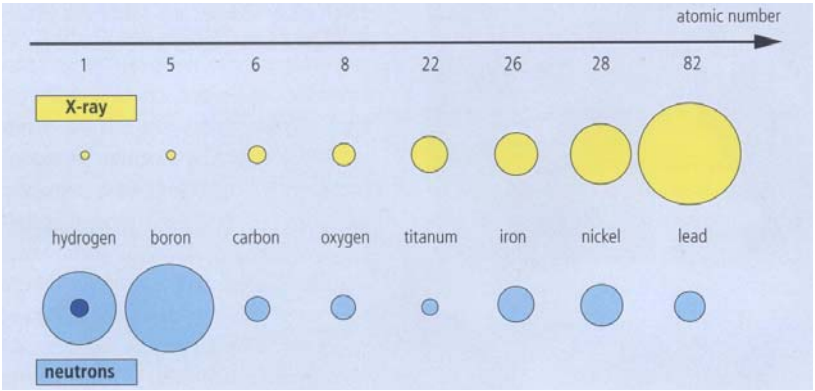

Fig. 28 Attenuation of X-rays and thermal neutrons by different elements (size of the circles), in case of hydrogen elastic scattering (large circle) dominates above absorption (small circle), source: PSI [29]

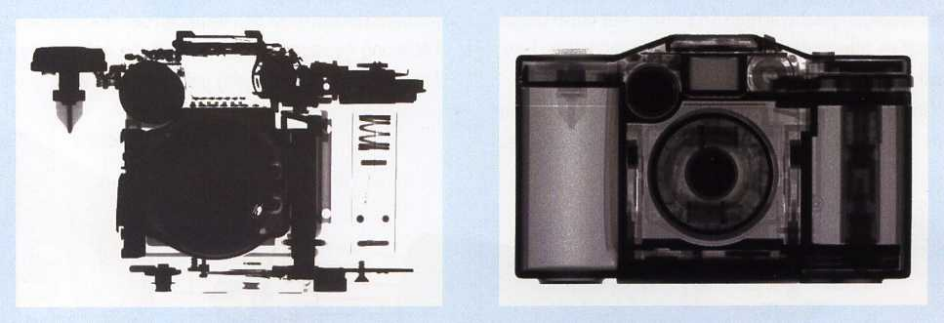

Fig. 29 Radiogramme of a mirror reflex camera, left: X-rays, right: neutrons, source: PSI [29]

The application of neutrons is especially fruitful, when the fluid is practically non-transparent for photons, like in case of liquid heavy metals, which became interesting in connection with the development of ADS and PbBi cooled fast reactors. Neutrons can transit even through considerably thick layers of such a melt and give good contrast with the gas phase [30]. It has to be noted that the strength of the neutron source defines the time resolution. As it can be seen from Fig. 30, a thermal flux of $1.5 \cdot 10^8$ 1/(cm²·s) is sufficient to achieve frame rates of several 100 Hz, but with increasingly spoiling signal-to-noise ratios.

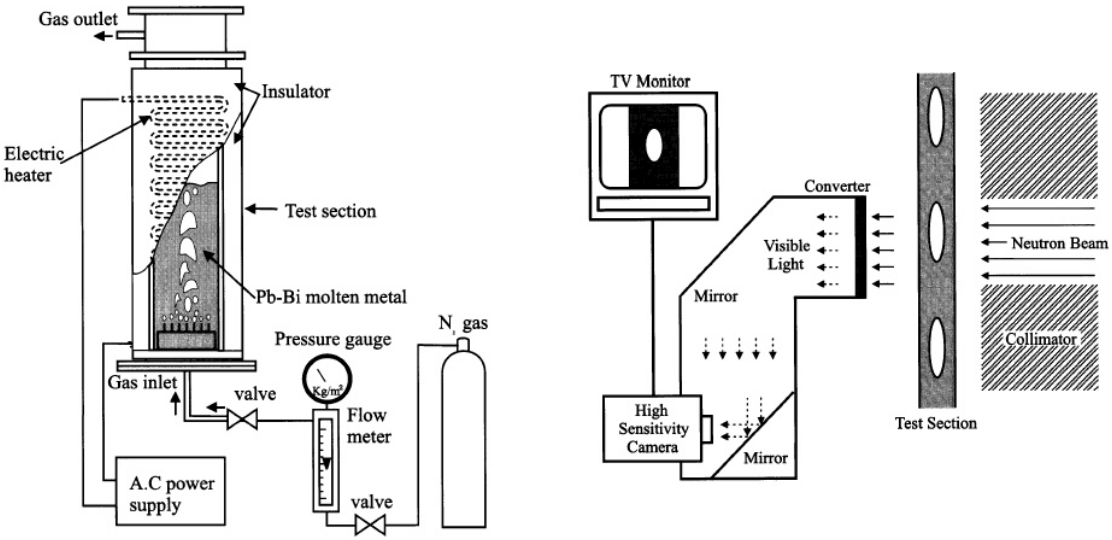

Fig. 30 Experimental set-up (left) and neutron radiography arrangement (right) used by Mishima & Hibiki [30] for gas - liquid metal studies

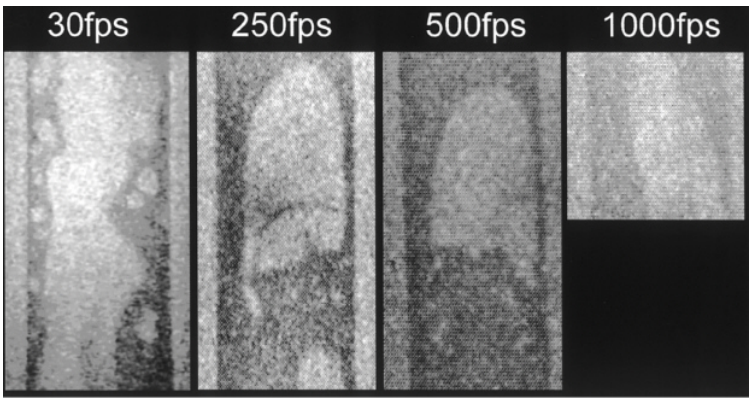

Fig. 31 Raw imaging quality of gas bubbles in Pb-Bi molten metal as a function of exposure time in case of a steady-state thermal neutron flux of $1.5 \cdot 10^8$ 1/(cm²·s) obtained from the JRR-3M research reactor of JEARI at a thermal power of 20 MW [30]

Saito & Mishima [31] used the same radiography set-up to measure gas bubbles and liquid velocity field simultaneously in a heavy metal natural circulation loop. The latter was done using a particle tracking technique, for which neutron absorbing seeds from $AuCd_3$ (Cadmium is another strong absorber of thermal neutrons) were added to the fluid.

Another interesting application is steam explosions. The interaction of droplets of molten heavy metal with water was imaged by Saito et al. [32]. In order to limit the attenuation of the water to get a good

contrast it was substituted by D_2O, which has lower cross-sections. Images taken at 500 Hz suffer from quite strong noise, but still reveal details in the fragmentation of the jet and steam production and rise (Fig. 32), especially if improved by off-line filtering [33].

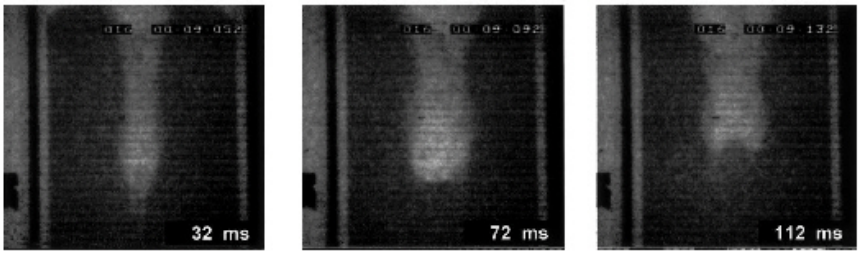

Fig. 32 Selected images of heated stainless-steel particle and heavy water interaction (recording speed: 500 frames/s, particle temperature: 1000 °C, particle diameter: 12 mm) [32].

Tomography can only be carried out, if the object can be rotated, since available strong neutron beams come from a big, stationary installation (reactor, spallation source) that cannot be rotated around the object. This is a considerable limitation to a wide application. Fast tomography with neutrons similar to the achievements in ultrafast X-ray tomography seems to be infeasible, since an electronic rotation of the source would require the neutrons to be deflectable by electrostatic or magnetic fields, which is not the case; or to generate them as a secondary radiation of deflectable and controllable beams of other particles, for which no realistic solutions are at hand.

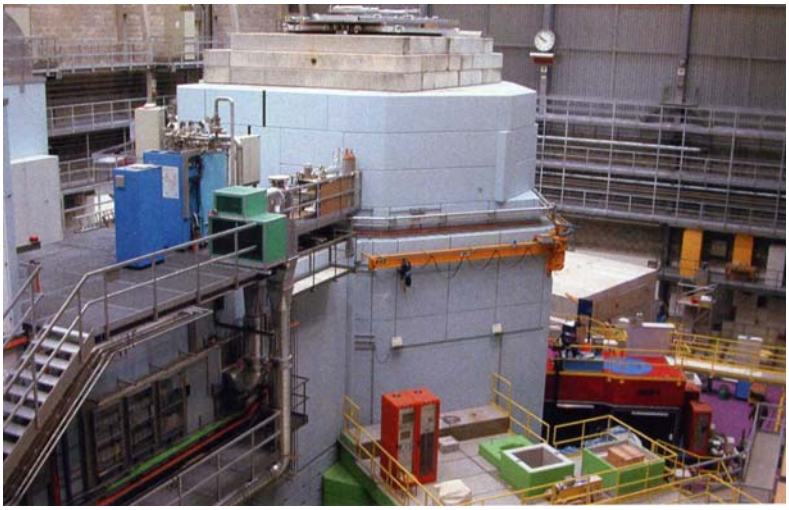

Fig. 33 Spallation source at PSI, Switzerland, thermal flux in the transmission radiography channel: $3.4 \cdot 10^6$ 1/(cm²·s), ∅350

Remember, that even transmission radiography requires heavy equipment, like high-flux research reactors or spallation sources (Fig. 33) to generate the necessary neutron fluxes. Nevertheless, some innovative potentials can be attributed to the use of neutrons in fluid dynamics studies, especially if new strong radiography beams can be involved, like thermal beam line ANTARES of the FRM-II [34] with fluxes of 10^8 1/(cm²·s) of thermal and alternatively cold neutrons.

11. Magnetic Resonance Imaging

Widely used in medical diagnostics is the method of Magnetic Resonance Imaging (MRI), which is based on the effect of nuclear magnetic resonance. The method is non-intrusive and can deliver distributions of the nuclear density of isotopes the nuclear spin of which is different from zero. Most prominent nuclide is hydrogen, less frequently used ones are, among others, deuterium, carbon 13, nitrogen 14. The technique can be organized to acquire space averaged, local as well as distributed information on 1D, 2D or 3D domains.

Basically, the spin of nucleus performs a precession movement when put into a magnetic field. This is accompanied with the irradiation of a radio frequency signal. The frequency of the precession is called

Larmor frequency and is proportional to the strength of the magnetic field, where the proportionality factor is specific for each nuclide.

A macroscopic amount of identical nuclei can produce a significant and detectable radiofrequency pulse, when the precession of many nuclei is synchronized. This is done by transmitting a radiofrequency pulse (a so-called 90 deg RF pulse) to the object to be studied. Resonance conditions are necessary, i.e. the spins in only those parts of the object are synchronized, which find themselves in a region, were the frequency corresponds to the Larmor frequency for the local magnetic field intensity (for hydrogen 42.58 MHz/T). In this way, a selective activation of a part of the object is possible, e.g. the labelling of a measuring cross-section in a flow channel. This is achieved by temporarily applying a gradient of the magnetic field to the object. The resonance conditions are then found only in a slice of the object, the thickness of which can be controlled by the intensity of the gradient and the bandwidth of the RF pulse. Gradients are created using coils additional to the magnet that generates the main field.

After the end of the activation pulse, the RF pulse generated by the synchronized precession is called free induction and can be received to characterize the amount of activated matter within the object. The amplitude of the signal is proportional to the number of nuclei that became affected by the pulse transmitted into the object, but also depends from the magnetic field intensity. It decreases rapidly for three reasons: the nuclei fall soon out of synchrony, and the spin polarization decreases in the directions of the magnetic field lines and perpendicular to them. This is called free induction decay. Since the loss of synchrony is the fastest and therefore dominating contribution to the free induction decay, the precession of the spins continues for a much longer time. Subsequent additional RF pulses sent into the object (so-called 180 deg pulses) can recover the synchronization and cause spin echoes to appear. A measurement based on their evaluation is called spin-echo technique. This is crucially for any imaging, since the time lag between the free induction decay and the appearance can be used to code the position within the object by applying a magnetic field gradient in a direction different to the field gradient applied during activation. Spins at positions with higher field intensity rotate faster, therefore the position along the field gradient and thus within the activated slice is coded in the phase of the received echo signal. Another field gradient perpendicular to the latter one, which is put during the receive of the echo pulse modifies the Larmor frequency according to the position in the third direction. In this way, 3D imaging becomes a task of an inverse Fourier transformation of the received signals.

Unfortunately, the phase coding requires repetition of the described echo sequence with a variation of the gradient strength during the phase coding. This, and the fact that often ensemble averaging of receiver signals is necessary to obtain the needed statistical reliability of the signals, lead to comparatively large imaging time. The method is therefore first of all suitable for steady state measurements.

It is always possible to omit the coding in certain directions to come to the measurement of a density averaged over a 1D, 2D or 3D domain. In this case, the spin-echo sequence simplifies and, usually, the measuring rates can be increased. This is quite often applied in fluid dynamics studies found in literature.

It is a striking advantage of MRI that it is perceptible not only to the density of a given nuclide species, but also to the velocity in case of moving objects. To explain the principle: A portion of fluid activated by a 90 deg pulse in slice defined by a field gradient carries the precessing nuclei a certain distance downstream, before the echoes are recorded. Now the nuclei find themselves in locations where the gradient is different and therefore the velocity is coded in the emitted Larmor frequency, or, depending on the type of applied spin-echo sequence, in the phase of the RF signal.

A nice example for an application of this technique to a bubbly flow was published by Leblond [35]. The MRI device used a main magnetic field in axial direction of a pipe (Fig. 34). A gradient was applied in flow direction, too. In this way, slices of the fluid in a measuring cross-section were

activated. Due to the displacement of the fluid along the field gradient according to the local velocity, the echo contained the information about the probability density distribution of the liquid phase, since the gaseous phase did not contribute to the spin echo. The overall intensity of the echo is proportional to the total amount of liquid activated. This allowed an additional void fraction measurement. Due to the 1D configuration, imaging was not possible.

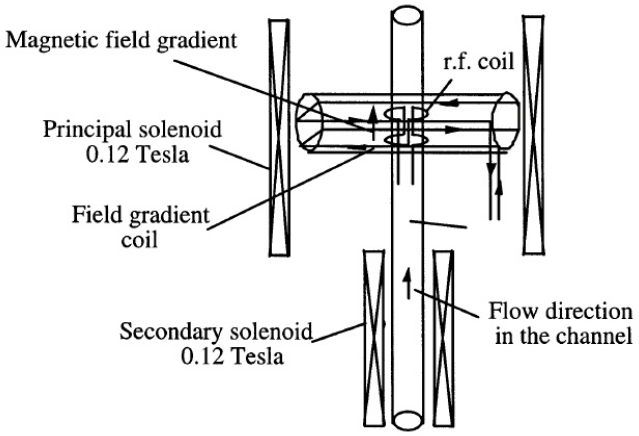

Fig. 34 1D set-up for MRI of a vertical pipe flow [35, 36]

As the result, PDFs of the liquid velocity in dependency from the gas fraction were recorded. The influence of the bubbles, especially the wake of them, to the liquid motion is recognizable in the increasing width of the PDFs (Fig. 35).

Later, the same device was used by Barberon & Leblond [36] to study the axial void distribution in large Taylor bubbles (i.e. the part of the cross-section occupied by the Taylor bubble) and to obtain the PDF of the water velocity at different parts and in the wake of the bubble (Fig. 36).

It has to be remarked that this very nice result was obtained by an ensemble averaging procedure from data that was acquired over 10 h. To that end the Taylor bubbles were periodically reproduced by a special gas injection device as much accurate as possible. This was necessary due to the bad signal-to-noise ratio of the NMR setup, which was equipped with a main coil producing a 0.12 T field only.

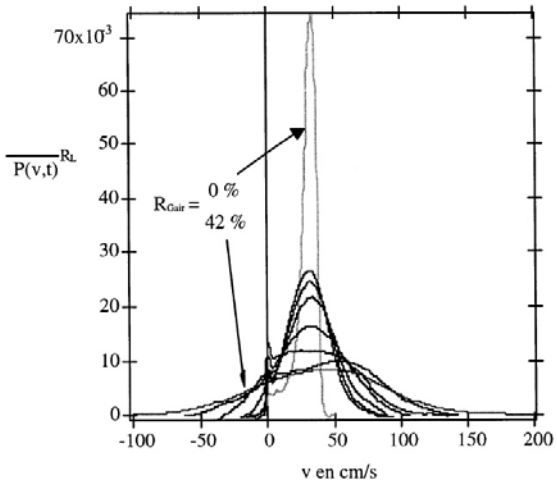

Fig. 35 PDFs of the liquid velocity in a bubbly flow, turbulence enhancement with growing gas fraction (0 - 42 %), MRI results, [35]

Furthermore, the measurement of the polarization decay can reveal information about the temperature. Chemical bindings can be studied by utilizing the so-called chemical shift, i.e. the slight variations of the Larmor frequency caused by the influence of the fields of neighbouring atoms to the precessing nucleus. The latter soon collides with the need of field gradients for imaging, that's why chemical shift measurements are often performed without spatial resolution (NMR Spectroscopy).

Applications, where real transient 2D or 3D tomographic imaging was performed, are restricted to slow flows of very viscous fluids, pastes or capillary flows in porous bodies. Here, the imaging rates offered by standard MRI devices are sufficient. Examples can be found in [37 - 39].

There is a way to speed-up the data acquisition by applying a only one re-synchronizing 180 deg pulse to produce a strand of gradient echoes from only one single activation pulse. For this, very fast changing transient fields are necessary, which is a challenge to the driving circuits for the gradient coils. In this way, a full cycle of gradient variation can by reduced to very small periods. The technique is called Echo-planar Imaging (EPI, Mansfield, Nobel prize in 2003, [40]). Typical repetition rates are in the range of some milliseconds. Achieving the necessary high data quality

requires high main field intensities, which leads to superconducting electromagnets. During the fast sequence gradients have to be switched in very short times, which requires very powerful driving circuits for the gradient coils. Both is quite a challenge and makes the method very costly. The next step is Echo Volume Imaging (EVI) with even higher requirements to the hardware.

In two-phase fluid dynamics, EPI was used to obtain sequences of 2D liquid distributions in a horizontal duct in the regime of slug flow [41]. The achieved imaging period was 7 ms (framing rate ~140 Hz). It is clearly recognisable, that higher imaging frequencies are a big challenge for the future development of MRI techniques.

Remember furthermore, that MRI relies on well-defined magnetic field conditions inside the object and on fast changing fields. Both magnetic and conducting materials are therefore forbidden in the object and in a considerable region around it. Flows in metallic pipes or fuel rod bundles etc. can therefore not be studied. This restricts the application mostly to some fundamental studies. Nevertheless, and despite of the high costs of the equipment, MRI is a promising method for CFD code validation, since the capability of a fully non-intrusive velocity measurement (seeds for PIV or particle tracking may distort a two-phase flow, too, see [42]) can be combined with void detection in one and the same device.

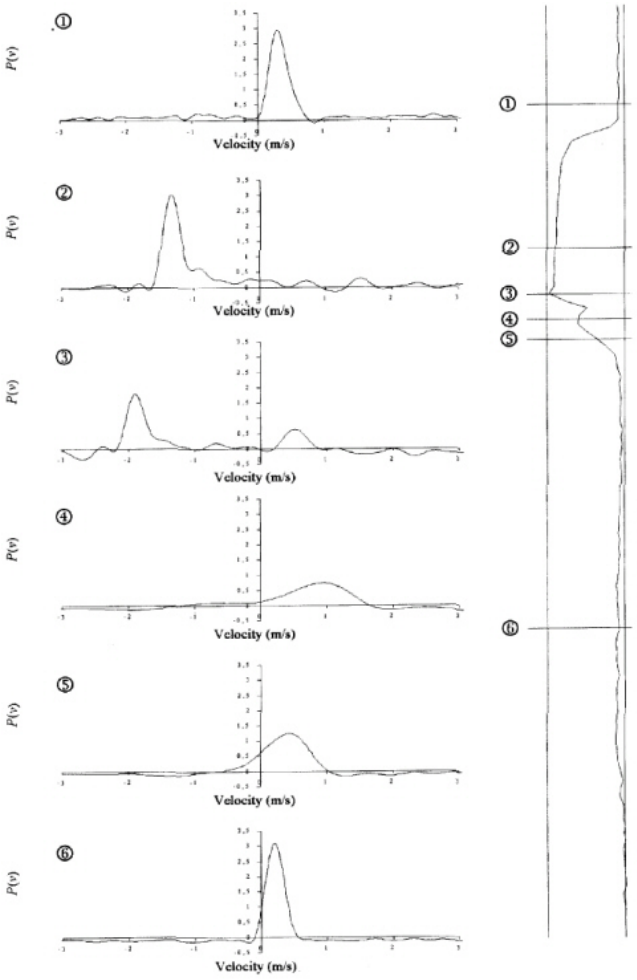

Fig. 35 MRI produces PDFs of the liquid velocity in different positions of a large Taylor bubble in a vertical slug flow, [36]

12. Diving Chamber Technology

Free optical access to high-pressure flows was the initial motivation to develop the so-called "Diving Chamber Technology" for performing steam-water experiments at up to 5 MPa under pressure equilibrium. TOPFLOW in Rossendorf was equipped with a pressure chamber, which used as containment for the test facility itself. The tank has an inner diameter of about 2.5 m and a length of 7 m (Fig. 36). At the front side, it is equipped with a quick-opening full-size port that allows fast access to the test facility inside.

Experiments can be carried out with steam-water mixtures at saturation temperature corresponding to the operation pressure of 5 MPa. The steam comes from the TOPFLOW heater (4 MW, appr. 1.7 kg/s). The exhaust stream from the test section is condensed in a built-in heat exchanger which is connected to the cooling water system of TOPFLOW. This condenser has a permanent connection to the inner atmosphere of the tank from its cold end. In this way, the pressure in the test section is kept at the same level as the pressure in the tank, which is pressurized by a compressor system. The inner

atmosphere has to be cooled in order to maintain a maximum temperature of 50 °C, which is the operation limit for the tank and for many types of instrumentation put directly in the tank. If, for the reason of a cooling failure, the temperature in the tank rises above 70 °C, an emergency shut-down of the steam supply is activated.

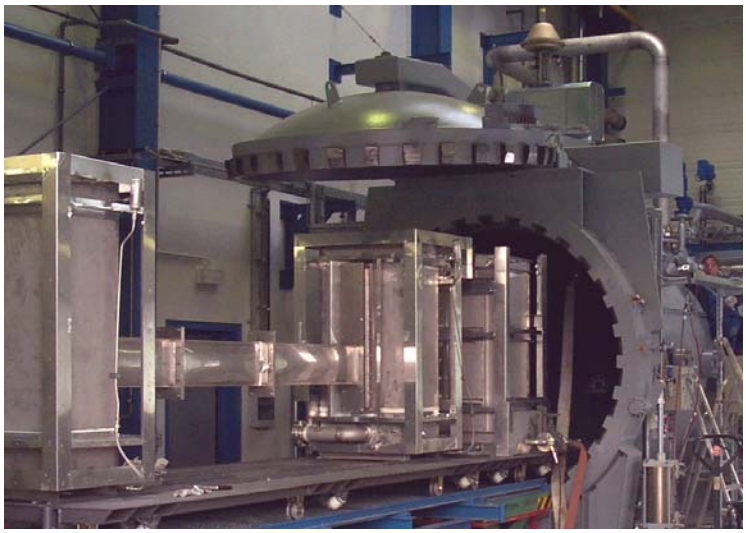

Fig. 36 TOPFLOW "Diving Chamber", view from the side of the full-size port, hot-leg test without thermal insulation and still without steam generator inlet chamber

The first experiment which was planned was a PWR hot-leg test for the visualisation of the dynamic free surface between water and steam in the inlet chamber of a PWR steam generator during reflux-condenser mode close to the counter current flow limitation point. For this purpose, a horizontal test channel with a semi-circular flat model of the steam generator entrance chamber was built (Fig. 37). It is put between two separator vessels of rectangular cross-section. The region of the steam generator inlet has glass walls on both sides that allow full optical access to the flow. A high-speed camera accommodated in a small pressure-proof container is pointed to this part of the test section. Diffuse backlight is used for illumination, produced by LED panels, which were found to withstand the ambient of the pressure tank without additional measures. The tank together with the test section is shown in Fig. 38.

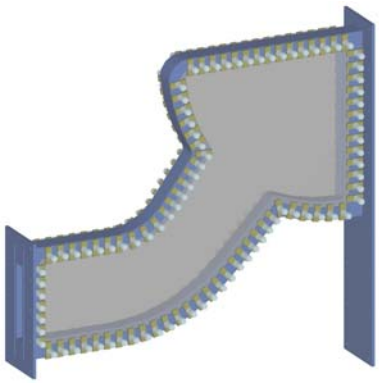

Fig. 37 Flat model of a PWR steam generator inlet chamber with glass walls

Fig. 38 contains also a schematic view of the built-in condenser. The heat exchanger tubes are vertically oriented. Inlet and outlet collectors for the cooling water are horizontal pipes at the bottom of the condenser tank. Steam coming from the test section enters the condenser from the top. At the cold U-tubes, it is condensed and a stable stratification layer is formed between the steam on top and air at the bottom, since the density of air at 5 MPa is significantly higher than the steam density. This stratification layer may move up and down in dependency on the steam flow rate to be condensed, i.e. the heat exchanger surface is adapting to the steam supply by a self regulation mechanism, which was successfully demonstrated.

The Diving Chamber is a universal facility that can house different test sections. The test section is mounted on a movable tray that can be extracted from the tank via the full-size port. Flange connections inside the tank are foreseen for the media supply. High pressure steam and water can be transported in flexible stainless steel hoses, which is a special feature due to the pressure equilibrium.

An important issue is a sufficient thermal insulation of the test section to avoid heat losses to the inner atmosphere of the tank, which would heat-up the pressurized atmosphere in the tank above the allowed limits. Here, we were confronted with essential problems, since some of the traditional insulation materials, like mineral wool and glass wool failed due to the decrease of kinematical viscosity of air with increasing pressure. As a consequence, natural circulation starts inside the fibre mats, when the

pressure in the tank is high. Alternatives tested were foam glass and a self-inflating silicon resin. Foam from the latter material was used to insulate the test section. It has very good and stable insulation properties and is fully fire-resistant at ambient atmospheric pressure. During a test at 5 MPa, the silicon foam nevertheless started burning, causing limited damage to the facility. The destruction of the insulation led to a delay in the research programmes and a suspension of the hot-leg test. The decision was taken to inertialize the tank using nitrogen for the pressurization in the future.

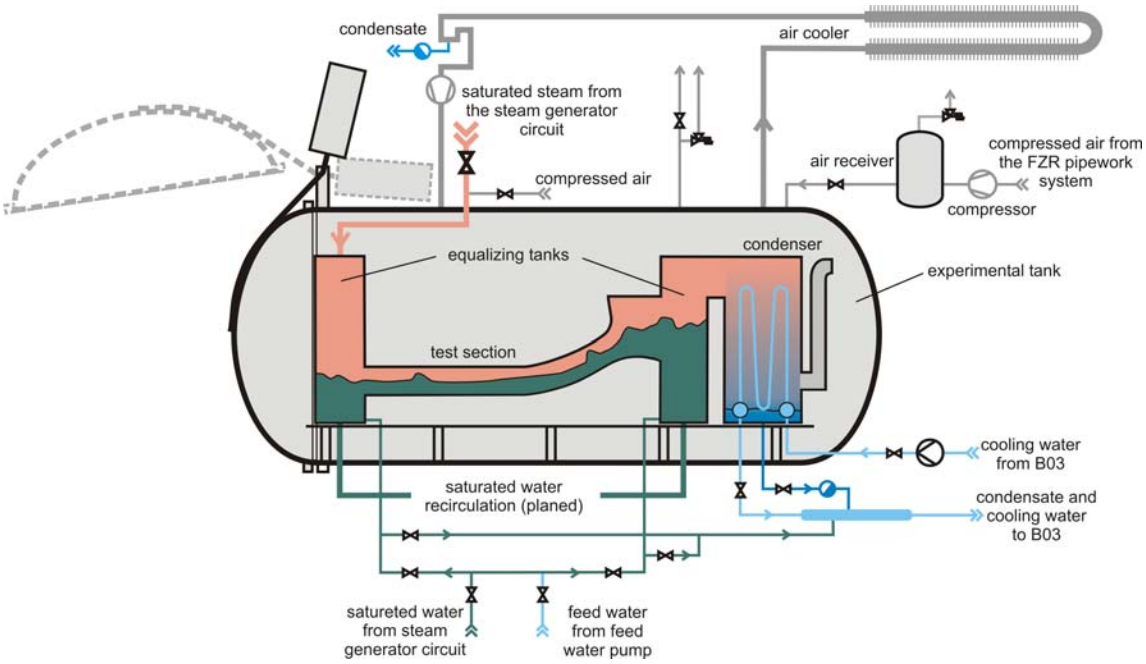

Fig. 38 TOPFLOW pressure tank "Diving Chamber" with hot-leg test to study free-surface flow in the primary circuit of a PWR during reflux condenser mode

13. TOPFLOW-PTS experimental programme

During a Loss-Of-Coolant Accident (LOCA), ECCS/accumulator cold water is injected into the cold leg, which may result in crucial Pressurized Thermal Shocks (PTS) on the structural components, first of all the Reactor Primary Vessel (RPV) wall. The concern is to reliably predict/assess the thermal loads on the RPV wall, and it's an actual issue today in view of the aging and plant life time extension. In case of some small break LOCA transients, cold water can be injected into a partially (or totally) uncovered cold leg, thus resulting in a specific two-phase flow configuration involving a dispersed two-phase flow in the cold water impinging jet area and a downstream stratified two-phase flow along the cold leg to the RPV down-comer, and possibly in the down-comer.

The refined analysis of the latter configuration has concluded the open medium 3D CFD modeling of two-phase flows would enable a more accurate and reliable prediction of the temperature load on the RPV wall, as soon as the modeling is correctly validated with respect to the industrial configurations. In that prospect, the "TOPFLOW-PTS Experimental Program" has been designed; its objective is to provide a well informed experimental data base to further:

- perform validation/assessment of the complete related CFD modeling including wall-to-fluid heat transfer (mainly along the down-comer wall);
- improve the understanding of the key physical involved thermal-hydraulics phenomena (mainly direct contact condensation and liquid phase turbulence in the impinging jet and stratified flow areas), as well as the development and/or closure and validation of the related models.

The TOPFLOW-PTS Experimental Program, jointly operated by CEA, EDF, Framatome-ANP, FZR, IRSN and PSI, is an integral-type program which accounts for a correct relevance of the experimental configurations with respect to the industrial application ones, both from a geometrical and thermal-hydraulics point of view; it involves:

- a 1:2.5 scaled down mock-up representing a part of one cold leg and down-comer of the French CPY 900 MWe reference plant; the cold leg is modeled as a straight pipe whereas the down-comer is planar and represents a 90° angle sector of the original down-comer. This mock-up will be operated inside the TOPFLOW "Diving Tank" under pressure equilibrium conditions;
- experiments with (*i*) full and partial sub-cooling of the ECC injection water, (*ii*) nearly saturated conditions (injection of saturated water), (*iii*) water injection in air environment, to check the impact of mass transfer and gas-to-liquid density ratios on the two-phase flow dynamics. Water-steam tests will be carried out at pressures up to 50 bars.

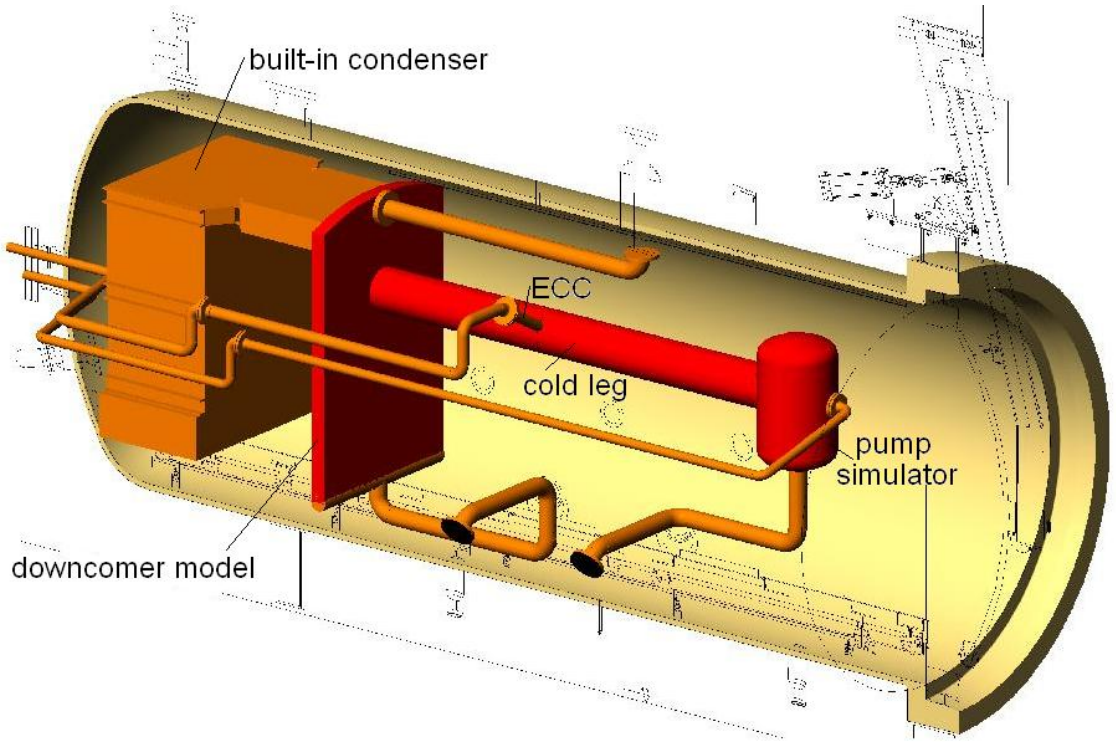

Fig. 39 TOPFLOW-PTS test section installation inside the pressure tank "Diving Chamber", preliminary design

Based on the instrumentation related issues and the current state of the art for the measurement techniques to provide the required local data, the TOPFLOW-PTS Experimental Program does include 3 stages:

- *a Stage 1 involving the use of today mature techniques*, namely thermocouple lances/matrices along the cold leg and down-comer, pairs of wire–mesh sensors in the impinging jet area and along the cold leg, a high-speed camera and an IR camera, as well as a "heat flux probe" over half a part of the down-comer outer wall. Furthermore, TC-void probes are expected to be implemented in the mock-up;

- *a Stage 2 related to the further development/qualification of two promising techniques for the current thermal-hydraulic conditions: Particle Image Velocimetry (PIV) and a four-tip electrical probe,* to additionally provide local data;
- *a Stage 3, with the implementation of the two previous measurement techniques,* in case Stage 2 will have demonstrated their actual applicability and reliability.

TOPFLOW-PTS will benefit from the advantages of the Diving Chamber technique: The test section can be designed without the need to stabilize it against large overpressure, otherwise non-pressurizable geometries become feasible, novel opportunities for instrumentation will be offered, like the measurement of the wetted temperature of the inner RPV wall using an infrared observation from the outside (the IR camera will be put in the pressure tank), and - last but not least - a limitation of the costs.

The commissioning of the mock-up and its instrumentation (Stage 1) is planned for 2007, whereas the actual tests will be performed in the second half of 2007; the statements with respect to the anticipated use of a four-tip electrical probe and PIV will be supported by the begin of 2008. Stage 3 would be carried out later on.

14. Summary

A large part of tasks for CFD in nuclear reactor safety concerns 3D simulations of mostly transient gas-liquid two-phase flows in large components, at high thermodynamic parameters, often with the presence of fast interfacial mass transfer, where the occurring void fractions cover the entire range from plain liquid to plain steam. Fortunately, CFD has generalizing properties that allow to transfer the applicability of closure relations from one geometry to another, as long as the main participating phenomena are reflected. Experiments for code validation and model development can therefore depart from a full geometric similarity of the flow domains to be studied, which was still necessary for the closure relations for thermal hydraulic modelling. This may ease the life of the experimenters, since good accessibility for instrumentation can be taken into account during the design of test facilities.

On the other hand, closure relations for CFD or better C(M)FD have to be formulated on a microscopic, geometry-independent level of the calculation cell. The necessary new quality of empirical knowledge creates new requirements towards instrumentation. It is no more sufficient to measure mass, momentum and energy balances between inlet and outlet domains of components that have to be reflected in a 1D plant model, but flow quantities have to be measured in a distributed way on grids that have a similar discretization as the calculation grids of the codes. This is a big challenge, especially if experiments at close-to-power-plant conditions are needed.

Some progress was made by the introduction of wire-mesh sensors that represent a step in the right direction. They are suitable for gas-liquid flows in parameter regions where other methods fail, which are the working horses in cases with low loadings of the particulate phase (bubbles, solids), like PIV, optical particle / bubble tracking, LIF, LDA, or which are not stable enough in hostile environments, like optical needle probes, hot film probes and similar. Contactless methods are emerging, which can compete with the mesh sensors or can overtake them in terms of the resolution. This is above all X-ray tomography with deflected electron beams or multiple X-ray generators, and partially gamma tomography. Neutrons for radiography and the use of MRI techniques are other potential candidates, though they are not without natural limitations.

Optical methods including IR cameras for temperature measurements may get better access to flows at high pressure, when the TOPFLOW "Diving Chamber" will be fully operational. This multi-purpose test facility is open for external users, too. The planned TOPFLOW-PTS programme is a good example for a multilateral cooperation benefiting from this experimental infrastructure.

Acknowledgements

Presented results of own research activities of the author were obtained together with colleagues from Forschungszentrum Rossendorf, Institute of Safety Research under the lead of Frank-Peter Weiss. To the presented material contributed by name Matthias Beyer, Helmar Carl, Heiko Pietruske, Peter Schütz and the technical crew of the TOPFLOW facility, Thomas Höhne, Eckhard Krepper, Dirk Lucas, Annalisa Manera and Ulrich Rohde from the theoretical group, Arnd Böttger, Jochen Zschau, Uwe Hampel, Cornelius Zippe, Winfried Zippe and many others from the group of instrumentation development, and the team of ROCOM, Gerhard Grunwald, Sören Klim, Tobias Sühnel and others. The author thanks all these colleagues from Rossendorf for the inspiring, productive and enthusiastic time. Wire-mesh sensor electronics were developed together with the TELETRONIC GmbH in Rossendorf (www.tz-rotech.de/teletronic/).

References

[1] Prasser, H.-M., Böttger, A., Zschau, J.: A New Electrode-Mesh Tomograph for Gas-Liquid Flows, Flow Measurement and Instrumentation 9 (1998) 111-119.

[2] Prasser, H.-M., Krepper, E., Lucas, D.: Evolution of the Two-Phase Flow in a Vertical Tube - Decomposition of Gas Fraction Profiles according to Bubble Size Classes using Wire-Mesh Sensors, International Journal of Thermal Sciences 41 (2002) pp. 17-28.

[3] Prasser, H.-M., Misawa, M., Tiseanu, I.: Comparison between wire-mesh sensor and ultra-fast X-ray tomograph for an air-water flow in a vertical pipe, Flow Measurement and Instrumentation 16 (2005) 73-83.

[4] Prasser, H.-M., Beyer, M., Böttger, A., Carl, H., Lucas, D., Schaffrath, A., Schütz, P., Weiß, F.-P., Zschau, J.: Influence of the pipe diameter on the structure of the gas-liquid interface in a vertical two-phase pipe flow, Nuclear Technology 152(2005)Oct, 3-22.

[5] Vanga, B. N. R., Zaruba, A., Krepper, E. Prasser, H.-M.: Experimental investigation of the hydrodynamics of confined bubble plumes in water and viscous media, NURETH-11, Avignon, France, October 2-6, 2005, paper 456.

[6] Prasser, H.-M., Scholz, D., Zippe, C.: Bubble size measurement using wire-mesh sensors, Flow Measurement and Instrumentation 12/4 (2001) 299-312.

[7] Pietruske, H., Prasser, H.-M.: Wire-mesh sensors for high-resolving two-phase flow studies at high pressures and temperatures, Flow, NURETH-11, Avignon, France, October 2-6, 2005, paper 533.

[8] Dudlik, A., Prasser, H.-M., Apostolidis, A., Bergant, A.: Water hammer induced by fast acting valves - experimental studies at Pilot Plant Pipework, Multiphase Science and Technology (submitted).

[9] Prasser, H.-M., Grunwald, G., Höhne, T., Kliem, S., Rohde, U., Weiss, F.-P.: Coolant mixing in a PWR - deboration transients, steam line breaks and emergency core cooling injection - experiments and analyses, Nuclear Technology 143 (2003) 37-56.

[10] Prasser, H.-M., Höhne, T., Kliem, S., Rohde, U., Weiß, F.-P.: Untersuchung der Kühlmittelvermischung an der Versuchsanlage ROCOM - Experimente und Modellierung, Fachsitzung "Experimentelle und theoretische Untersuchungen zu Borverdünnungstransienten in DWR" auf der Jahrestagung Kerntechnik 2003, Berlin, 20.-22. Mai 2003, Proceedings INFORUM S.57-83.

[11] Kliem, S., Sühnel, T., Rohde, U., Höhne, T., Prasser, H.-M., Weiss, F.-P.: Experiments at the Mixing Test Facility ROCOM for Benchnarking of CFD Codes, OECD/IAEA workshop CFD4NRS, Garching, September 5 – 7 , 2006, session A4, paper 17.

[12] Lenka, S. N., Prasser, H.-M., Durst, F., Ajmani, S. K., Bhattacharjee, D.: Advanced Mixing Studies in Hydrodynamic Models of Steelmaking Vessels, Metallurgical and Material Transactions B (submitted).

[13] Prasser, H.-M., Beyer, M., Carl, H., Gregor, S., Lucas, D., Pietruske, H., Schütz, P., Weiss, F.-P.: Evolution of the Structure of a Gas-Liquid Two-Phase Flow in a Large Vertical Pipe, NURETH-11, Avignon, France, October 2-6, 2005, paper 399.

[14] Tomiyama, A., 1998, Struggle with computational bubble dynamica, in: Proceedings of Third International Conference on Multiphase Flow, ICMF 98, Lyon, France, June 8-12, 1998.

[15] Frank, T., Zwart, P. J., Krepper, E., Prasser, H.-M., Lucas, D.: Validation of CFD Models for Mono- and Polydisperse Air-Water Two-Phase Flows in Pipes, OECD/IAEA workshop CFD4NRS, Garching, September 5 – 7 , 2006, session B6, paper 32.

[16] Manera, A., Lucas, D., Prasser, H.-M.: Experimental investigations on turbulent dispersion in a vertical large diameter pipe for bubbly and slug flow regimes by means of correlation techniques, NURETH-11, Avignon, France, October 2-6, 2005, paper 091.

[17] Sato, Y., Sekoguchi, K.: Liquid velocity distribution in two-phase bubble flow, International Journal of Multiphase Flow, 2, 79-95 (1975).

[18] Sato, Y., Sadatomi, M., Sekoguchi, K.: Momentum and heat transfer in two-phase bubble flow, International Journal of Multiphase Flow, 7, 167-177 (1981).

[19] Lucas, D., Prasser, H.-M.: Simulation of condensation in a sub-cooled bubbly steam-water flow along a large vertical pipe, Archives of Thermodynamics 26(2005)4, 49-59.

[20] Prasser, H.-M., Beyer, M., Carl, H., Frank, T., Pietruske, H., Schütz, P.: Gas-Liquid Flow Around an Obstacle in a Vertical Pipe - Experiments and CFD Simulation, Annual Meeting on Nuclear Technology, Aachen, May 16-18, 2006, proceedings pp. 93 - 98.

[21] A. Beisiegel, A., Kronenberg, J., Kreuter D.: Expanding the Test Capabilities of the Multifunction Thermal Hydraulic Test Loop KATHY, Annual Meeting on Nuclear Technology, Aachen, May 16-18, 2006, paper 321, pp. 131-134.

[22] Bieberle, A.; Hampel, U.; Schleicher, E.; Hoppe, D.; Prasser, H.-M.; Sühnel, T.; Zippe, C.: Design and performance of a high-resolution gamma tomography device, 4th World Congress on Industrial Process Tomography, 05.09.-08.09.2005, Aizu, Japan.

[23] Bieberle, A.: Messung der Dampfgehaltsverteilung in Brennelementbündeln mittels eines neuen hochauflösenden Gammatomographen, Jahrestagung Kerntechnik, Aachen, 16.-18. Mai 2006, Vortrag auf Kompetenzerhaltungsprogramm.

[24] Prasser, H.-M., Baldauf, D., Fietz, J., Hampel, U., Hoppe, D., Zippe, C., Zschau, J., Christen, M., Will, G.: Time Resolving Gamma-Tomography for Periodically Changing Gas Fraction Fields, Flow Measurement and Instrumentation 14 (2003)3 pp. 119-125.

[25] Hampel, U., Hoppe, D., Diele, K.-H., Fietz, J., Höller, H., Kernchen, R., Prasser, H.-M., Zippe, C.: Application of gamma tomography to the measurement of fluid distributions in a hydrodynamic coupling, Flow Measurement and Instrumentation 16 (2005) 85-90, 2005.

[26] Boyd, D.P., Lipton, M.J., Cardiac computed tomography, Proc. IEEE, 71 (1983) 298–307.

[27] Hori, K., Fujimoto, T., Kawanishi, K., Nishikawa, H.: Advanced High Speed X-Ray CT Scanner for Measurement and Visualization of Multi-Phase Flow, OECD/CSNI Specialist Meeting, Santa Barbara (CA), 1997.

[28] Hampel, U., Speck, M., Koch, D., Menz, H.-J., Mayer, H.-G., Fietz, J., Hoppe, D., Schleicher, E., Zippe, C., Prasser, H.-M.: Ultrafast X-ray Computed Tomography with a Linearly Scanned Electron Beam Source, Flow Measurement and Instrumentation 16 (2005), 65-72.

[29] Neutron Radiography at the Spallation Neutron Source SINQ of the Paul Scherrer Institute, public information material, PSI, Dec. 2001.

[30] Mishima K., Hibiki, T.: Development of high-frame-rate neutron radiography and quantitative measurement method for multiphase flow research, Nuclear Engineering and Design 184 (1998) 183–201.

[31] Saito, Y., Mishima, K., Tobita, Y., Suzuki, T., Matsubayashi, M.: Visualization and Measurements of Velocity Fields and Void Fraction in Gas-liquid Metal Two-Phase Flow by Neutron Radiography, 4th International Conference on Multiphase Flow, May 27 - June 1, 2001, New Orleans, USA, paper 866.

[32] Saito Y., Mishima K., Hibiki, T., Yamamoto, A., Sugimoto, J., Moriyama K.: Application of high-frame-rate neutron radiography to steam explosion research, Nuclear Instruments and Methods in Physics Research A 424 (1999) 142-147.

[33] Mishima, K., Hibiki, T., Saito, Y., Nishihara, H., Tobita, Y., Konishi, K., Matsubayashi, M.: Visualization and measurement of gas-liquid metal two-phase flow with large density diference using thermal neutrons as microscopic probes, Nuclear Instruments and Methods in Physics Research A 424 (1999) 229-234.

[34] Grünauer, F.: Image reconstruction and multiple hole apertures in neutron radiography at FRM-II, Nuclear Instruments and Methods in Physics Research A, article in press.

[35] Leblond, J., Javelot, S. Lebrun, D., Lebon, L.: Two-phase flow characterization by nuclear magnetic resonance, Nuclear Engineering and Design 184(1998)229-237.

[36] Barberon, F., Leblond, J.: Intermittent two-phase flow study by NMR, C. R. Acad. Sci. Paris, Chimie / Chemistry 4(2001)853-856.

[37] Götz, J., Zick, K., Kreibich, W.: Possible optimisation of pastes and the according apparatus in process engineering by MRI flow experiments, Chemical Engineering and Processing 42 (2003) 517-534.

[38] Gladden, L.F., Lim, M.H.M., Mantle, M.D., Sederman, A.J., Stitt, E.H.: MRI visualisation of two-phase flow in structured supports and trickle-bed reactors, Catalysis Today 79–80 (2003) 203–210.

[39] Barnes, E.C., Wilson, D.I., Johns, M.L.: Velocity pro filing inside a ram extruder using magnetic resonance (MR)techniques^, Chemical Engineering Science 61 (2006)1357–1367.

[40] Mansfield, P. Multi-planar image formation using NMR spin echoes. J Phys C. 10:L55-L58. 1977.

[41] Reyes, J.N., Lafi, A.Y., Saloner, D.: The use of MRI to quantify multi-phase flow patterns and transitions: an application to horizontal slug flow, Nuclear Engineering and Design 184 (1998) 213–228.

[42] Minagawa, H., Yamada, R., Takano, Y., Shakutsui, H.: Effect of fine particles added into gas-liquid two-phase slug flows in a vertical pipe, HEAT 2002, Baranov Sandomierski, Poland, June 24-27, 2002, proceedings on CDROM.